1   # Development of an aerosol chemical transport model RAQM2

2   # and predictions of Northeast Asian aerosol mass, size,

3   # chemistry, and mixing type.

4

5   M. Kajino[1, 2], Y. Inomata[3], K. Sato[3], H. Ueda[4], Z. Han[5], J. An[5], G. Katata[6], M. Deushi[1],

6   T. Maki[1], N. Oshima[1], J. Kurokawa[3], T. Ohara[7], A. Takami[7], and S. Hatakeyama[8]

7   [1]{Meteorological Research Institute, Japan Meteorological Agency, 1-1 Nagamine,

8   Tsukuba 305-0052, Japan}

9   [2]{Pacific Northwest National Laboratory, P.O.Box 999 Richland WA 99352, USA}

10   [3]{Asia Center for Air Pollution Research, 1182 Sowa, Nishi, Niigata 950-2144, Japan}

11   [4]{Toyohashi Institute of Technology, 1-1 Hibarigaoka, Tempaku, Toyohashi 950-2144,

12   Japan}

13   [5] {Institute of Atmospheric Physics, Chinese Academy of Sciences, Beijing 100029, China}

14   [6] {Japan Atomic Energy Agency, 2-4 Shirakata-shirane, Tokai, Ibaraki 319-1195, Japan}

15   [7] {National Institute for Environmental Studies, 16-2 Onogawa, Tsukuba 305-8506, Japan}

16   [8] {Tokyo University of Agriculture and Technology, 3-5-8 Saiwaicho, Fuchu, Tokyo 183-

17   8509, Japan}

18   Correspondence to: M. Kajino (kajino@mri-jma.go.jp)

19

20   Short title: Development of RAQM2 and Asian aerosol mixing type simulation

21

22

23

24

1   Abstract

2   A new aerosol chemical transport model, Regional Air Quality Model 2 (RAQM2), was

3   developed to simulate Asian air quality. We implemented a simple version of a triple-moment

4   modal ~~moment~~ aerosol dynamics model (MADMS) and achieved a completely dynamic (non-

5   equilibrium) solution of a gas-to-particle mass transfer over a wide range of aerosol diameters

6   from 1 nm to super μm. To consider a variety of atmospheric aerosol properties, a category

7   approach was utilized, in which the aerosols were distributed into 4 categories: particles in

8   Aitken mode (ATK), soot-free particles in accumulation mode (ACM), soot aggregates

9   (AGR), and particles in coarse mode (COR). In the current setting, aerosol size distribution in

10   each category is characterized by a single mode. Condensation, evaporation, and Brownian

11   coagulations for each mode were solved dynamically. A regional-scale simulation ($\Delta x = 60$

12   km) was performed for the entire year of 2006 covering the Northeast Asian region. ~~Statistical~~

13   ~~analyses showed that the model reproduced the regional-scale transport and transformation of~~

14   ~~the major inorganic anthropogenic and natural air constituents almost within factors of 2 to 5.~~

15   The modeled PM_1/bulk ratios of the chemical components were consistent with the

16   observations, indicating that the simulated aerosol mixing types were consistent with those in

17   nature. Non-sea salt SO_4^{2-} mixed with ATK + ACM was the largest at Hedo in summer,

18   whereas it mixed with AGR was substantial in cold seasons. Ninety-eight percent of the

19   modeled NO_3^- was mixed with sea salt at Hedo, whereas 53.7% of the NO_3^- was mixed with

20   sea salt at Gosan, located upwind toward the Asian continent. The condensation of HNO_3

21   onto sea salt particles during transport over the ocean makes the difference in the NO_3^-

22   mixing type at the two sites. Because the aerosol mixing type alters optical properties and

23   cloud condensation nuclei activity, its accurate prediction and evaluation are indispensable for

24   aerosol-cloud-radiation interaction studies.

25

28

29

30

31

1 Introduction

Atmospheric trace gases and aerosols have various detrimental effects on ecosystems and human health. Because their emission, secondary formation, transport and deposition mechanisms are highly complex and still unknown, a great number of studies on the development and application of air quality modeling are ongoing. Recently, Jacobson and Ginnebaugh (2010) developed a global-through-urban nested three-dimensional air pollution model that implements a large explicit photochemical mechanism with 4,675 gases and 13,626 tropospheric and stratospheric chemical reactions. The mechanism also includes one internally mixed aerosol and three hydrometeor categories that are size and chemistry resolved (17 components × 14 size bins for aerosols, 18 components × 30 size bins for cloud/precipitation liquid, cloud/precipitation ice, cloud/precipitation graupel). On the other hand, there is still a high demand for computationally efficient models for the purpose of long-term integration with higher grid resolutions. For example, the Community Multiscale Air Quality (CMAQ) model (Byun and Schere, 2006) was extensively used worldwide and was continually updated for more than 10 years to the current version 4.7 (Foley et al., 2010).

Asian air quality is highly complex because it covers the tropics to the polar zones with huge amounts of anthropogenic air pollutants and natural Asian dust particles together with other natural species. The Regional Air Quality Model (RAQM) was developed at the Acid Deposition and Oxidant Research Center (currently changed to the Asia Center for Air Pollution Research), which focuses on such Asian air quality problems (An et al., 2002; Han, 2007). The model has been used for various air pollution studies in Asia, such as studies on high oxidant, massive dust transport, and volcanic sulfur episodes, and substantial modifications have been made based on comparison and evaluation with extensive and long-term monitoring data (An et al., 2002, 2003; Han, 2007; Han et al., 2004, 2005, 2006; Kajino et al., 2004, 2005) and with other models (Carmichael et al., 2008 and references therein). However, an aerosol dynamics module was not implemented in RAQM, and thermodynamic equilibrium was assumed for the gas-aerosol partitioning of semi-volatile inorganic components such as sulfate, nitrate and ammonium.

To simulate the evolutionary processes of aerosol microscale properties such as chemical compositions, size distribution and mixing state, we implemented a simple version of a new modal-moment aerosol dynamics model (Kajino, 2011; Kajino and Kondo, 2011) that enables

the non-equilibrium calculation of gas-to-particle mass transfer over a wide range of aerosol diameters from 1 nm to super-micrometer particles. We also implemented six important parameterizations relating to aerosol dynamics: 1. new particle formation, 2. cloud condensation nuclei (CCN) activation, 3. ice nuclei (IN) activation, 4. an explicit grid-scale cloud microphysical module, 5. dry deposition, and 6. sub-grid-scale convection and scavenging.

The new model is referred to as RAQM2. In Sect. 2, a unique aerosol dynamics module is described in detail together with the above parameterizations. The model results are evaluated in Sect. 3 using the Acid Deposition Monitoring Network in East Asia (EANET) and the Cape Hedo Atmosphere and Aerosol Monitoring Station (CHAAMS). The major findings are summarized in Sect. 4.

2   Model description

2.1   General description of the WRF/RAQM2 framework and parameterizations used in the models

In this section, a general description of an offline-coupled meteorology – chemical transport framework (WRFV3/RAQM2) is presented; however, because the aerosol dynamics model of RAQM2 is unique, it is described in detail in Sect. 2.2. Table 1 summarizes the list of data and schemes used in the WRF and RAQM2 models.

Fig. 1 illustrates the model domain of WRF and RAQM2, and the locations of the observation sites of the Acid Deposition Monitoring Network in East Asia (EANET) and the Cape Hedo Atmosphere and Aerosol Monitoring Station (CHAAMS). There are horizontally 90×60 grids with 60km grid resolution on a Lambert conformal map projection. There are vertically 28 layers from the ground to 100 hPa for WRF and 13 layers to 10 km for RAQM2 with terrain-following coordinates. The horizontal grid points are common to both WRF and RAQM2, whereas the vertical grid points are different. After the spline vertical interpolation of wind velocity and air density to the RAQM2 levels, the mass balance is not maintained. Thus, the mass continuity model MSCWM (Ishikawa, 1994) is used to reduce the mass divergence due to the vertical interpolation to about 10^{-5} to 10^{-6} (s^{-1}). The input/output time interval for WRF-RAQM2 was set to 1 h. For the lateral and upper boundary concentrations of the RAQM2 simulation, the climatological simulation results of monthly NO_x, O_x, CO and volatile organic

compound (VOC) concentrations were used using a global-scale stratospheric and troposphere chemistry climate model (MRI-CCM2; Deushi and Shibata, 2011). The entire simulation period was 1 year, but each simulation was performed separately for each month (as most of the boundary data sets are on monthly basis), with a spin-up period of 2 weeks for RAQM2. WRF simulation was done for a year at once with a spin-up period of 3 days.

RAQM2 incorporates major processes for atmospheric trace species, such as anthropogenic and natural emissions, advection, turbulent diffusion, photochemistry, new particle formation, condensation, evaporation, Brownian coagulation, dry deposition, grid-scale cloud condensation nuclei (CCN) and ice nuclei (IN) activation and subsequent cloud microphysical processes, grid-scale aqueous chemistry in hydrometeors as well as in aerosol water, subgrid-scale convection and wet scavenging (Table 1).

The emission inventory was obtained from REAS (Ohara et al., 2007), which was extended to the year 2005 (Kurokawa et al., 2009). The emitted species are NO_x, SO_2, NH_3, NMVOCs (Non-Methane Volatile Organic Compounds), BC (Black Carbon), and POAs (Primary Organic Aerosols). Because REAS does not provide seasonal variations of the emission flux, we applied the simple monthly variations for Chinese emissions (Table 9 of Zhang et al., 2009). The temporal variations of the anthropogenic emission flux are not considered in the current setting. We used the Global Fire Emissions Database (GFED3; Giglio et al., 2010) for open biomass burning emissions (NO_x, SO_2, NMVOCs, BC and, POA) and the Model of Emissions of Gases and Aerosols from Nature (MEGAN2; Guenther et al., 2006) for biogenic emissions (isoprene and terpenes). Clarke et al. (2006) was used for sea salt production and Han et al. (2004) for the dust deflation process. The fractions of crustal elements such as Na^+, Ca^{2+}, Mg^{2+}, and K^+ in sea salt and Asian dust particles are derived from Song and Carmichael (2001). However, using the above combinations, the PM_{10} and non-sea salt (nss) Ca^{2+} were overestimated during the dust transport season in spring 2006 in Japan. There have been substantial efforts to adjust dust emission flux and transport by developing sophisticated physical deflation models (Kang et al., 2011, and references therein) or by applying state-of-the-art data assimilation techniques (e.g., Yumimoto et al., 2008; Sekiyama et al., 2010). Because deducing the accurate dust emission flux was not a focus of this study, we simply reduced the dust emission to one quarter uniformly in time and in space and the Ca^{2+} contents (6.8 wt%) in the Asian dust to half (3.4 wt%) to roughly adjust to both the observed PM_{10} and the nss-Ca^{2+} concentration at the Japan EANET stations for 2006. The value of 3.4 wt% is

1 smaller than that in previous works, such as Song and Carmichael (2001) and Wang et al.
2 (2002), but the value is still plausible compared with the China-map project data (available at
3 http://www.cgrer.uiowa.edu/EMISSION_DATA/biogeo/Ca-chinamap.gif).

4 The SAPRC99 mechanism (Carter, 2000) was implemented for gas phase photochemistry,
5 together with additional Secondary Organic Aerosol (SOA) formation mechanism (Edney et
6 al., 2007). However, because the contribution of SOA mass produced by the model was found
7 to be less significant to the East Asian regional-scale simulations and because we focused
8 mainly on the behaviors of inorganic components, the process was not included in the current
9 study. The aqueous phase chemistry in grid-scale cloud and rain water droplets as well as
10 aerosol water was considered (Walcek and Taylor, 1986; Carlton et al., 2007). The wet
11 scavenging due to the subgrid-scale convection was considered using the Asymmetrical
12 Convective Model (Pleim and Chang, 1992), whereas aqueous phase chemistry in convective
13 clouds was not considered. Zhang et al. (2003) was used to calculate the dry deposition
14 velocities of gaseous species. The monthly composite MODIS/LAI data processed from
15 MOD15A2 (available from https://lpdaac.usgs.gov/products; Myneni et al., 2002; Yang et al.,
16 2006) are used to obtain realistic values for the surface resistances of the dry deposition
17 velocity. Aerosol dry deposition is calculated using the method of Zhang et al. (2001) with
18 modifications to improve the prediction accuracy, as described in detail in Sect. 2.2.8.

2.2 Formulations of a fully dynamic aerosol module

20 The current aerosol module is a three moment bulk dynamics model that conserves number,
21 surface area, and mass concentrations of aerosol populations under the assumption that sizes
22 of aerosols can be represented by uni-modal lognormal size distributions (LNSDs). In this
23 section, an aerosol category approach is introduced that presents dynamical and chemical
24 evolutions in the mass and size distributions of aerosols due to emissions, new particle
25 formation, condensation, Brownian coagulation, dry deposition, CCN activation, IN
26 activation, and cloud microphysical processes using a modal-moment dynamics approach.

2.2.1 Simple version of a triple-moment aerosol module MADMS

28 A simple version of a triple-moment aerosol module called Modal Aerosol Dynamics model
29 for multiple Modes and fractal Shapes (MADMS; Kajino, 2011) was implemented in
30 RAQM2. MADMS can simulate the Brownian coagulation of a couple of modes with very

1 different LNSD parameters and with different mass fractal dimensions (D_f) of aggregates.

2 Simply, in RAQM2, all the particles were assumed to be spherical ($D_f = 3$).

3 As shown in Table 2, the populations of aerosols were grouped into 4 categories: 1. particles

4 in Aitken mode (ATK); 2. soot-free particles in accumulation mode (ACM); 3. soot

5 aggregates (AGR); and 4. particles in coarse mode (COR). The ATK category represents an

6 assemblage of aerosols formed by new particle formation and growing through the

7 coagulation and condensation of trace gases and water vapor. The ACM category includes a

8 part of the ATK aerosols that evolved to be larger than a certain diameter (set as 40 nm in this

9 study) as well as organic compounds and unidentified mass, and it excludes BC particles. The

10 AGR category indicates soot aggregates generated through combustion, and it contains BC

11 particles. Therefore, the ATK and ACM are non-light-absorbing particles, whereas AGR are

12 light-absorbing particles. Without separating the AGR category from the others, the evolution

13 of the mixing state of BC particles cannot be considered, which alters the absorption of solar

14 radiation and the number of CCN particles. The COR category includes mechanically

15 produced natural aerosols such as dust and sea salt particles as well as unidentified

16 components from PM_{10} emissions.

17 The aerosol sizes in each category were assumed to be characterized by a uni-modal LNSD.

18 There are three parameters ~~were used~~ to characterize the LNSD function: the number

19 concentration N, the geometric mean diameter D_g, and the geometric standard deviation σ_g.

20 Instead of the three parameters, in the modal-moment dynamics modeling, the temporal

21 evolutions of the three moments were solved to characterize the changes in the LNSD. The

22 kth moment is defined as

23

$$M_k = \int_{-\infty}^{\infty} D^k n(\ln D)\, d(\ln D) \tag{1}$$

24

Applying the Gaussian integral formula to Eq. (1) results in

25

$$M_k = N D_g^k \exp\left[\frac{k^2}{2} \ln^2 \sigma \right] \tag{2}$$

26 A list of transported species of each category is shown in Table 2. The zeroth and second

27 moments (M_0, M_2) and the mass concentrations of unidentified components (UIDs), BC, OA

28 (POA plus SOA), dust (DU), sea salt (except chloride) (SS), sulfate, ammonium, nitrate,

29 chloride and water are transported variables. By assuming a constant density of each chemical

composition, the M_3 of each category was diagnosed. More detailed derivations and descriptions of the modal moment approach are given in previous papers (e.g., Binkowski and Shankar; 1995; Whitby and McMurry, 1997; Kajino, 2011). Only the final forms of the equations, the time derivative terms of the moments, are shown in the current paper. How moments and the LNSD parameters are changed in the process operators are described later in Sect. 2.2.10 and Fig. 2b.

2.2.2 Intra-modal Brownian coagulation

The time derivative of moments due to intra-modal coagulation in the free-molecular regime can be expressed as

$$\frac{dM_0}{dt}\bigg|_{fm} = -bK_{fm}\left[M_0 M_{0.5} + M_2 M_{-1.5} + 2M_1 M_{-0.5}\right] \tag{3a}$$

$$\frac{dM_6}{dt}\bigg|_{fm} = 2bK_{fm}\left[M_3 M_{3.5} + M_5 M_{1.5} + 2M_4 M_{2.5}\right] \tag{3b}$$

where $K_{fm} = \left(\dfrac{3k_B T}{\rho_p}\right)^{0.5}$, k_B is the Boltzmann constant, T is temperature [K], and ρ_p is the

particle density. b is an approximation function of σ as

$$b(\sigma) = 1 + 1.2\exp(-2\sigma) - 0.646\exp(-0.35\sigma^2) \tag{4}$$

The time derivative terms in the near-continuum regime is

$$\frac{dM_0}{dt}\bigg|_{nc} = -K_{nc}\left[M_0 M_0 + M_1 M_{-1} + A\lambda M_0 M_{-1} + A\lambda M_1 M_{-2}\right] \tag{5b}$$

$$\frac{dM_6}{dt}\bigg|_{nc} = 2K_{nc}\left[M_3 M_3 + M_4 M_2 + A\lambda M_3 M_2 + A\lambda M_4 M_1\right] \tag{5b}$$

where $K_{nc} = \dfrac{2k_B T}{3\mu}$, A=2.492, μ is the viscosity of air, and λ is the mean free path of air molecules (cm). Finally, the harmonic mean of the time derivative terms in the free-molecular and near-continuum regimes is applied to cover the full size range of aerosols as

$$\frac{dM_k}{dt} = \frac{dM_k}{dt}\bigg|_{fm} \times \frac{dM_k}{dt}\bigg|_{nc} \bigg/ \left[\frac{dM_k}{dt}\bigg|_{fm} + \frac{dM_k}{dt}\bigg|_{nc}\right] \tag{6}$$

During the intra-modal coagulation, the third moment proportional to the total volume remains unchanged,

$$\frac{dM_3}{dt} = 0 \tag{7}$$

2.2.3 Inter-modal Brownian coagulation

Rules for the transfer of the three moments and chemical mass concentrations from one mode to another must be predefined for the inter-modal coagulation calculations. These rules are listed in Table 3. Basically, the moments and masses are transferred from smaller/simpler categories into larger/multiple-component categories. Assuming that when a particle in mode i coagulate with a particle in mode j, the merged particle goes into mode j (see Table 3), the time derivative terms of the moments in the near-continuum regime can be written as

$$\frac{dM_0^i}{dt}\bigg|_{nc} = -K_{nc}\left[2M_0^i M_0^j + M_1^i M_{-1}^j + M_{-1}^i M_1^j + A\lambda M_0^i M_{-1}^j + A\lambda M_{-1}^i M_0^j + A\lambda M_1^i M_{-2}^j + A\lambda M_{-2}^i M_1^j\right]$$

$$\frac{dM_3^i}{dt}\bigg|_{nc} = -K_{nc}\left[2M_3^i M_0^j + M_4^i M_{-1}^j + M_2^i M_1^j + A\lambda M_3^i M_{-1}^j + A\lambda M_2^i M_0^j + A\lambda M_4^i M_{-2}^j + A\lambda M_1^i M_1^j\right]$$

$$\frac{dM_6^i}{dt}\bigg|_{nc} = -K_{nc}\left[2M_6^i M_0^j + M_7^i M_{-1}^j + M_5^i M_1^j + A\lambda M_6^i M_{-1}^j + A\lambda M_5^i M_0^j + A\lambda M_7^i M_{-2}^j + A\lambda M_4^i M_1^j\right] \tag{8}$$

$$\frac{dM_0^j}{dt}\bigg|_{nc} = 0, \quad \frac{dM_3^j}{dt}\bigg|_{nc} = -\frac{dM_3^i}{dt}\bigg|_{nc}$$

$$\frac{dM_6^j}{dt}\bigg|_{nc} = K_{nc}\left[2M_6^i M_0^j + M_7^i M_{-1}^j + M_5^i M_1^j + A\lambda M_6^i M_{-1}^j + A\lambda M_5^i M_0^j + A\lambda M_7^i M_{-2}^j + A\lambda M_4^i M_1^j\right]$$

$$+ 2K_{nc}\left[2M_3^i M_3^j + M_4^i M_2^j + M_2^i M_4^j + A\lambda M_3^i M_2^j + A\lambda M_2^i M_3^j + A\lambda M_4^i M_1^j + A\lambda M_1^i M_4^j\right]$$

where M_k^i indicates the kth moment of mode i. In the free-molecular regime, the equations can be written as

$$\left.\frac{dM_0^i}{dt}\right|_{fm} = -bK_{fm}\left[M_0^i M_{0.5}^j + M_{0.5}^i M_0^j + M_2^i M_{-1.5}^j + M_{-1.5}^i M_2^j + M_1^i M_{-0.5}^j + M_{-0.5}^i M_1^j\right]$$

$$\left.\frac{dM_3^i}{dt}\right|_{fm} = -bK_{fm}\left[M_3^i M_{0.5}^j + M_{3.5}^i M_0^j + M_5^i M_{-1.5}^j + M_{1.5}^i M_2^j + M_4^i M_{-0.5}^j + M_{2.5}^i M_1^j\right]$$

$$\left.\frac{dM_6^i}{dt}\right|_{fm} = -bK_{fm}\left[M_6^i M_{0.5}^j + M_{6.5}^i M_0^j + M_8^i M_{-1.5}^j + M_{4.5}^i M_2^j + M_7^i M_{-0.5}^j + M_{5.5}^i M_1^j\right] \qquad (9)$$

$$\left.\frac{dM_0^j}{dt}\right|_{fm} = 0, \qquad \left.\frac{dM_3^j}{dt}\right|_{fm} = -\left.\frac{dM_3^i}{dt}\right|_{fm}$$

$$\left.\frac{dM_6^j}{dt}\right|_{fm} = bK_{fm}\left[M_6^i M_{0.5}^j + M_{6.5}^i M_0^j + M_8^i M_{-1.5}^j + M_{4.5}^i M_2^j + M_7^i M_{-0.5}^j + M_{5.5}^i M_1^j\right]$$
$$+ 2bK_{fm}\left[M_3^i M_{3.5}^j + M_{3.5}^i M_3^j + M_5^i M_{1.5}^j + M_{1.5}^i M_5^j + M_4^i M_{2.5}^j + M_{2.5}^i M_4^j\right]$$

where the approximation function b, newly proposed by Kajino (2011), is

$$b = 1 + 1.2\gamma \exp\left[-2\frac{\sigma_i + \alpha\sigma_j}{1+\alpha}\right] - 0.646\gamma \exp\left[-0.35\frac{\sigma_i^2 + \alpha\sigma_j^2}{1+\alpha}\right]$$

$$\gamma = \left[1 - \frac{\sqrt{1+\alpha^3}}{1+\sqrt{\alpha^3}}\right] \Bigg/ \left[1 - \frac{1}{\sqrt{2}}\right], \qquad \alpha = \frac{D_{gj}}{D_{gi}} \qquad (10)$$

The harmonic mean of the time derivative terms (Eq. 6) is applied to cover the full size range.

2.2.4 Number concentration of soot collided to coarse mode particles

Soot particles sometimes form internal mixture with coarse mode particles such as dust and sea salt particles, and such mixtures alter optical properties of the coarse mode particles significantly and contribute to atmospheric solar heating and surface dimming (Clarke et al., 2004; Zhu et al., 2007; Guazzotti et al., 2011). Such mixtures can be predicted in the RAQM2 model as BC mass and M_0^{AGR} number concentrations in the COR category (Table 2). M_0^{AGR} indicates the number concentration of soot particles (AGR) collided with COR particles and is calculated as

$$\frac{dM_0^{AGR}}{dt} = \left.\frac{dM_0}{dt}\right|_{coag}^{COR-AGR} \qquad (11)$$

M_0^{AGR} exceeds the M_0 of COR because M_0^{AGR} does not indicate the number of COR particles internally mixed with soot but indicates the number of times each AGR particle hits COR particles. Brownian coagulation theory assumes the coalescence efficiency is unity, but it may

1 not be true for the atmospheric aerosols. The efficiency of the bouncing/sticking of colliding

2 atmospheric particles should be formulated.

3

2.2.5 Condensation

5 The zeroth moment M_0 (=N) remains constant during the condensation process.

6
$$\frac{dM_0}{dt} = 0 \tag{12}$$

7 The condensational growth of the particle mass M of each mode can be expressed as

8
$$\frac{dM}{dt} = \int \frac{m_{w,p}}{m_{w,g}} (c_\infty - c_s) \psi(d_p) n(d_p) dd_p \tag{13}$$

9 where $m_{w,p}$ and $m_{w,g}$ represent the molecular weights of semi-volatile components in the

10 particle and gas phases, respectively, and c_∞ and c_s are the gas phase concentrations in the

11 bulk phase (near the aerosol surface) and those on the aerosol surface, respectively. The ψs

12 are different in the free-molecular and the near continuum regimes, which can be written as

13
$$\psi^{fm}(d_p) = \frac{\pi \alpha \bar{c}}{4} d_p^2 \tag{14a}$$

14
$$\psi^{co}(d_p) = 2\pi D_v d_p \tag{14b}$$

15 respectively, where α is a mass accommodation coefficient assumed constant as 0.1, $\bar{c}$ is a

16 mean velocity of the gas molecules, and D_v is the molecular diffusion coefficient. Using the

17 harmonic mean approach to cover the two regimes, the time derivative term of arbitrary

18 moments due to condensation can be rewritten as

19
$$\frac{dM_k}{dt} = \frac{1}{\rho_p} \frac{m_{w,p}}{m_{w,g}} (c_\infty - c_s) \left| \frac{k \alpha \bar{c}}{2} M_{k-1}, 4k D_v M_{k-2} \right|_{harm} \tag{15}$$

20 where $\left| A, B \right|_{harm}$ indicates the harmonic mean of A and B and, thus, AB/(A+B). The

21 condensational growth of mass is expressed as

22
$$\frac{dM}{dt} = \frac{\pi \rho_p}{6} \frac{dM_3}{dt} \tag{16}$$

1   To obtain the gas phase concentrations on the aerosol surface c_s, which is thermodynamically

2   equilibrated, ISORROPIA II (Fountoukis and Nenes, 2007) and Edney et al. (2007) are used

3   for semi-volatile inorganic and organic compounds, respectively.

4

5   ### 2.2.6 Simultaneous solution of nucleation, condensation and mode merging

6   RAQM2 achieved a completely dynamic (non-equilibrium) solution of a gas-to-particle mass

7   transfer over a wide range of aerosol diameters from 1 nm to super-micrometer size. The new

8   particle formation (NPF) process is, however, not dynamically solved, but parameterized,

9   which is inevitable for the time and spatial scales of the simulation. Recently, numerous NPF

10 parameterizations have been proposed based on laboratory experiments, theoretical and

11 molecular dynamics calculations, and nanoparticle observations (Kulmala and Kerminen,

12 2008; Hirsikko et al., 2011). However, numerous uncertainties and discrepancies remain

13 among each parameterization (Zhang et al., 2010). Therefore, we used the parameterizations

14 based on several observations in diverse atmospheric locations (Kuang et al., 2008) to obtain

15 the plausible nucleation rates for realistic conditions.

16 To solve the condensation onto the pre-existing particles and the nucleation of sulfuric acid

17 gas, the operator and time splitting method was applied. The nucleation and condensation

18 processes were solved simultaneously using the short split time step (Δt) of 1 sec with an

19 explicit method (forward in time) (see Section 2.2.9 and Fig. 2a). We found that a 1-sec time

20 step was sufficient to yield an accurate nucleation rate under the realistic conditions of

21 sulfuric acid gas up to 10^8 molecules (cm^{-3}) and aerosol number concentrations from 10^2 to

22 10^6 (cm^{-3}) using the Kuang et al. (2008) parameterization. When nucleation occurs, the

23 number of new particles, produced within 1 sec, with a D_g and σ of 1 nm and unity,

24 respectively, were entered in the ATK category. Because the ATK particles swelled rapidly

25 due to condensation and Brownian coagulations, the aerosols were merged to the larger

26 particle category ACM, as shown in Table 3. The portion of the kth moment larger than a

27 criteria diameter D_c were readily calculated using the error function erf(x) as

28

$$\left[M_k\right]_{D_c} = \int_{\ln D_c}^{\infty} D^k n(\ln D)\, d\ln D = \frac{M_k}{2}\left[1 - \mathrm{erf}\left(\frac{\ln D_c - \ln D_g - k \ln^2 \sigma}{\sqrt{2}\ln \sigma}\right)\right] \qquad (17)$$

The portion of mass is identical to that of the third moment. Each moment and each mass of the chemical compositions in ATK exceeding D_c (set as 40 nm in the study) were merged into the ACM category using Eq. (17), and vice versa: when the shrinking of the ACM occurs, the portion of the moments and mass smaller than 40 nm are merged to ATK (Table 3).

2.2.7   Grid-scale and sub-grid-scale wet deposition

For the grid-scale wet deposition, the CCN activation and subsequent cloud microphysical processes were parameterized using Abdul-Razzak and Ghan (2000) and WSM6 (Lin et al., 1983). When the Abdul-Razzak and Ghan (2000) parameterization predicts that CCN activation occurs in a grid cell, the portions of the moments and the mass (see Eq. (17)) were transferred to the grid-scale cloud droplets. Lin et al. (1983) developed an explicit cloud microphysics model in which interactions between cloud droplets and other hydrometers, such as rain, snow and graupel droplets, are formulated. The autoconversion rate (cloud → rain) and the accretion rate of cloud droplets by rain, snow, and graupel (cloud → rain, cloud → snow, cloud → graupel), predicted by WSM6, were used to calculate the transfer of the aerosol moments and mass in the cloud droplets to the other hydrometers.

Particles such as hydrophobic forms of dust and soot efficiently act as IN in ice and mixed phase clouds. Pagels et al. (2009) found that a mass increase of 2-3 times by the condensation of water and sulfuric acid onto soot agglomerates resulted in a transformation to spherical shapes. We assumed here that the soot loses IN activity after the growth by condensation. Thus, hydrophobic particles in RAQM2 are defined as AGR and COR categories when the hygroscopic mass (=sum of SO_4^{2-}, NH_4^+, NO_3^-, Cl^- and SS) is less than 50% of the total dry mass, i.e., the hygroscopic mass is less than the hydrophobic mass (=sum of UIC, BC, OA and DU).

All components in OA were assumed to be hydrophobic here, although some of the secondary OA was hydrophilic. For the IN activation of aerosols, we used the parameterizations of Lohmann and Diehl (2010) for contact freezing and immersion (+condensation) freezing. We assumed that the IN activation occurred only in a grid cell that contains ice particles predicted by WRF with a temperature lower than -3°C. The fractions of frozen droplets for dust and soot particles are assumed as functions of temperature based on Fig. 1 of Lohmann and Diehl (2010), respectively, as follows:

1
$$F_{cn\_du} = -14(T_c + 3)$$
$$F_{cn\_bc} = -15(T_c + 10)$$
$$F_{im\_du} = -0.1(T_c + 27)$$
$$F_{im\_bc} = -0.5(T_c + 36)$$

(18)

2 where F_{cn_du}, F_{cn_bc}, F_{im_du}, and F_{im_bc} represent the fractions for the contact freezing of

3 hydrophobic COR and AGR and the immersion freezing of hydrophobic COR and AGR,

4 respectively, and T_c is the grid air temperature (°C). For immersion freezing, the F_{im_du} and

5 F_{im_bc} are the exact fractions scavenged into ice particles. For contact freezing, some portion

6 of F_{cn_du} and F_{cn_bc} actually coagulated with ice or super-cooled cloud droplets can be

7 scavenged into ice particles. The Brownian coagulation of hydrophobic COR and AGR with

8 cloud ice/water droplets was calculated using the inter-modal coagulation Eqs. (6), (8), (9)

9 and (10). To obtain the size distribution of cloud ice/water droplets, we assumed a simple

10 Khrgian-Mazin-type gamma size distribution (Pruppacher and Klett, 1997):

11

$$n(a) = Aa^2 \exp(-Ba)$$

(19)

12 where n(a) is the number size distribution function, A and B are parameters related to

13 moments of the distribution, and a is a particle radius. This Khrgian-Mazin equation is almost

14 identical to the LNSD, with a standard deviation of approximately 1.64. Thus, assuming a D_g

15 of cloud ice/water droplets of 15 μm together with cloud ice/water mixing ratios and their

16 density, the size distribution can be fixed for the inter-modal Brownian coagulation.

17 Subsequently, aerosols in ice particles are converted to snow via autoconversion (aggregation)

18 and are converted to rain, snow and graupel particles due to accretion, with conversion rates

19 predicted by the explicit cloud microphysics parameterization (WSM6).

20 The below-cloud scavenging process is considered inter-modal coagulation with falling

21 hydrometers, such as rain, snow and graupel droplets. Kajino and Kondo (2011) deduced the

22 collision/coalescence equations due to gravitational settling in Eqs. (A37)-(A43) in section

23 A.4 of their paper. The LNSD is assumed in their equations, while the size distributions of

24 such hydrometers are often represented by a gamma function. Thus, we first derive the

25 gamma size distributions (GSDs) of the hydrometers as a function of the mixing ratio (Hong

26 and Lin, 2006) and then yield the LNSD converted from GSD, preserving the three moments.

Once captured in the hydrometeors in either ways, a certain portion of the moments and chemical components is assumed to immediately reach the ground in the same manner as Eqs.(1) and (2) in Kajino and Kondo (2011).

2.2.8 Dry deposition and gravitational sedimentation

The dry deposition and gravitational sedimentation processes are formulated in the same manner as that given in Appendices 5 and 6 of Kajino and Kondo (2011) through Eqs. (A44) to (A48). With regard to the calculation of dry deposition for particles, however, the original parameterization of surface resistance by Zhang et al. (2001) used in Kajino and Kondo (2011) was modified based on comparisons using observational data by more recent works (Katata et al. 2008, 2011; Petroff and Zhang 2010) to improve the prediction accuracy of dry deposition. In the present paper, four important revisions were performed:

1. On the assumption that forests have tall canopies and a large leaf surface area that enables a large amount of particles from the atmosphere to be captured, the empirical constant ε_0 in Zhang et al. (2001) was set to 5 and 1 for the categories of forest and short vegetation, respectively. This modification decreases the surface resistance, resulting in large values of dry deposition velocity for forest compared with other vegetation.

2. For the collection efficiency by leaves due to inertial impaction, the modified function of Peters and Eiden (1992) (Eq. (7) in Katata et al. 2008) was used. The function was validated with the data of fog deposition (> 1 μm) onto coniferous and broad-leaved forests in Katata et al. (2008).

3. Collection efficiencies due to interception and Brownian diffusion by Kirsch and Fuchs (1968) and Fuchs (1964) (Eqs. (14) and (16) in Katata et al. 2011), respectively, were also used for vegetative surfaces. Those formulations were verified using the flux data of fine aerosols (< 1 μm) over the coniferous forest in Katata et al. (2011).

4. For the land use categories of desert, tundra, ice cap and glacier, inland water, and ocean, the surface resistance for non-vegetated surfaces proposed by Petroff and Zhang (2010) were adopted.

After the above modifications, the dry deposition velocity calculated by the modified model agreed better with the observational data than the original model of Zhang et al. (2001). For

example, the size-segregated dry deposition velocity for the vegetative surface decreased and increased by one order of magnitude within a 0.1- and 1-μm-diameter range, which is comparable to the performance of the detailed multi-layer particle deposition model by Katata et al. (2011). For ground and water surfaces, a good agreement between calculations by the modified model and observations from the literature was found, as shown in Petroff and Zhang (2010).

2.2.9 Operator splitting and time splitting for aerosol dynamical modeling

The operator splitting and time splitting used for the aerosol dynamics module are illustrated in Fig. 2a. In the flow chart, each solid box indicates each operator, and the arrows denote the order of operator calculations. ΔT_{host} is the longest time step of the host calculation, i.e., horizontal advection and diffusion. In this study, we set $\Delta x = 60$ km, so $\Delta T_{h\text{ost}}$ is set as 300 sec after optimization of the CPU time and the deficit of numerical diffusions. Δt is a split time step within each operator calculation, whereas the ΔTs denote the integrated time steps of each operator before stepping forward to the next operator. First, the production rate of sulfuric acid gas via homogeneous (gas phase) chemistry was calculated using SAPRC99 with the Eulerian Backward Iteration method with $\Delta t = 150$ sec. The production rate of sulfuric acid gas was obtained as $\Delta C_{\text{H2SO4}} / \Delta T_{\text{host}}$. The nucleation rate $J_{1\text{nm}}$ (Kuang et al., 2008) and the condensation rate (Eqs. 15 and 16) were calculated using $C_{\text{H2SO4}} = \Delta C_{\text{H2SO4}}/\Delta T_{\text{host}} \times \Delta t$ (=1 sec). Then, the gas-phase concentration C_{H2SO4} was distributed into the ATK category to produce new particles and into all categories by condensation simultaneously. After finishing the NPF&Cond. operator, the intra- and inter-category Brownian coagulation was solved with an arbitrary split time to integrate for $0.5\Delta T_{\text{host}}$ (150 sec). CFL-like conditions were established for Brownian coagulation as

$$t_{CFL} = M_0^i \left/ \frac{dM_0^i}{dt} \right. \tag{20}$$

where Δt is set as the maximum so that it never exceeds $0.5 \times t_{CFL}$ for all the modes in the categories due to intra- and inter-category coagulations. After the Coag. operator is calculated for half the host time step, the condensation of the semi-volatile inorganic and organic components is calculated. The CFL conditions are also introduced for the condensation process as

$$t_{CFL} = 1/k_w \qquad (21)$$

where k_w is the mass-transfer coefficient (s^{-1}) for each mode defined as

$$k_w = \frac{dM}{dt}\frac{1}{(c_\infty - c_s)} \qquad (22)$$

and the time derivative of mass concentration dM/dt is obtained from Eqs. (15) and (16). Δt is set as the maximum so that it never exceeds $0.1 \times t_{CFL}$ for all modes of the categories. The condensation process was integrated for the host time step period (300 sec) with the arbitrary time step. After the volatile components condensation operator, the Coag. operator was calculated again for the remaining half of the host time step (150 sec). Other processes then follow, including sedimentation, dry deposition, subgrid-scale wet deposition, grid-scale CCN activation and cloud microphysics.

Strictly speaking, NPF, the condensation of sulfuric acid gas and other semi-volatile components, and Brownian coagulation should be solved with the smallest time step, i.e., 1 sec, to calculate the growth of aerosol particles consistently. However, although ISORROPIA2 is computationally efficient compared with other models (Fountoukis and Nenes, 2007), solving the thermodynamic equilibrium state among multi-component species for every 1 sec for all modes of the categories in the regional scale simulation is still far from feasible for our computational resources. To avoid operator split problems to some extent, the ΔT of the Brownian coagulation is divided in two and inserted separately between the two condensational operators in the current implementation of the model.

2.2.10 Time evolution of the moments and the LNSD parameters in each process operator

At any steps during the time integration, each mode of the categories has the specific size parameters (N, D_g, σ_g) to characterize their LNSD. Then M_0 and M_2 derived by Eq. 2, together with the chemical components (listed in Table 2) are transported via advection, turbulent diffusion, and sub-grid scale convection. Then, there are three moments after the transport operator, M_0, M_2 and M_3, which is diagnosed by total mass and predetermined density of each chemical component. Using the three moments, the size parameters (N, D_g, σ_g) after the transport operators are obtained by Eq. 2. This is the case for the transport

1 operators but in common for the aerosol process operators (Fig. 2a) too, as illustrated in
2 Fig.2b. To obtain dM_0/dt, dM_2/dt, and dM_3/dt for the condensation operator in Eq.15, any
3 moments necessary in the equation are derived by the size parameters. Using Eq.15, M_0, M_2
4 and M_3 after the condensation operator are obtained, and subsequently N, D_g and σ_g after the
5 operator. The same procedure is applied for other process operators such as sedimentation,
6 dry deposition, subgrid-scale wet deposition, grid-scale CCN activation and cloud
7 microphysics, except for the coagulation operator, where dM_6/dt needs to be calculated
8 instead of dM_2/dt (Eqs.3–10). In the coagulation operator too, any moments necessary for the
9 coagulation equations (Eqs.3–10) are derived by the size parameters N, D_g and σ_g before the
10 coagulation operator, M_0, M_3 and M_6 after the coagulation operator is obtained by the
11 equations, and then N, D_g and σ_g after the coagulation operator are derived.

12

13 ## 3   Model evaluation using observation data

14 ### 3.1   EANET monitoring network data

15 Acid Deposition Monitoring Network in East Asia (EANET) data were used for model
16 evaluation. The guidelines, technical documents, monitoring reports and quality assurance
17 and quality control programs are available at http://www.eanet.cc/product.html. We used
18 hourly SO_2, NO_x, O_3, $PM_{2.5}$ and PM_{10} concentrations and meteorological parameters, and 1-
19 or 2- weekly concentrations of gases (SO_2, NH_3, HNO_3, and HCl) and aerosols components
20 (SO_4^{2-}, NO_3^-, Cl^-, NH_4^+, Na^+, Mg^{2+}, K^+, and Ca^{2+}) using the filter pack method (FP). The
21 long-duration sampling of FP causes several artifact problems; volatilization of NH_4NO_3 and
22 NH_4Cl collected on a filter occur during sampling and/or high humidity may reduce measured
23 gas concentration due to trapping by condensed water in the filter pack. To avoid the
24 problems, only total nitrate (T-NO_3^-; HNO_3^- gas plus NO_3^- aerosol), total ammonium (T-
25 NH_4^+; NH_3 gas plus NH_4^+ aerosol), and total chloride (T-Cl^-; HCl gas plus Cl^- aerosol) are
26 used for in this study.

27 To obtain the anthropogenic SO_4^{2-} and Ca^{2+} originating from the Asian dust (calcite), nss-
28 SO_4^{2-} and nss-Ca^{2+} were defined, excluding the contribution of sea salt using a standard mean
29 chemical composition of sea water (DOE, 1994), as follows:

$$[\text{nss-SO}_4^{2-}] = [\text{SO}_4^{2-}] - 0.251 \times [\text{Na}^+]$$

(24)

$$[\text{nss-Ca}^{2+}] = [\text{Ca}^{2+}] - 0.038 \times [\text{Na}^+]$$

where [ ] denotes the weight concentrations in µg m^{-3}.

Among the EANET stations, six stations in Japan are selected for the model evaluation, as depicted in Fig. 1 and listed in Table 4. The red triangles denote the stations located on small islands or isolated capes in down-wind regions. These stations were situated in areas without nearby large anthropogenic emission sources and without the complexity of local orographic winds; therefore, high concentration episodes mostly coincided with synoptic-scale disturbances and were well simulated by regional-scale models. On the other hand, because those stations were very close to ocean surfaces, the regional-scale simulations of ocean-originated species such as sea salt did not often agree well with the observations. We often obtained a better agreement for sea salt-originated components at inland or mountainous stations.

3.2   Q-AMS aerosol observation data at the CHAAMS site

Because the temporal resolution of the ionic aerosol component measurements of EANET is 2 weeks, the simulated transport and transformation of aerosol components cannot be evaluated. Alternatively, we used the hourly concentrations of PM_1-nss-SO_4^{2-}, PM_1-NO_3^-, PM_1-Cl^-, and PM_1-NH_4^+ (50% cutoff of aerosols with an aerodynamic diameter of 1 µm), measured using a quadrupole aerosol mass spectrometer (Aerodyne Research Inc., Q-AMS) at the Cape Hedo Atmospheric and Aerosol Monitoring Station (CHAAMS) site (Takami et al., 2007; Takiguchi et al., 2008). The CHAAMS site is located within the same premises as the EANET Hedo station.

3.3   Bulk mass concentrations of gaseous species

It was necessary to predict the O_3 concentration precisely because it is an important oxidizing agent in the atmosphere for secondary aerosol formations. This prediction was also important because O_3 is a source of the most efficient oxidants in the troposphere, OH radicals. Because

1   O_3 is a relatively longer-lived species, the contribution of inter-continental transport and

2   stratospheric ozone intrusion is substantial (Sudo and Akimoto, 2007; Nagashima et al., 2010).

3   Consequently, the seasonal trends can never be reproduced by a tropospheric regional-scale

4   model itself without appropriate seasonal variations of the lateral and upper (tropopause)

5   boundary conditions. Therefore, we used the climatological simulation results of monthly

6   NO_x, O_x, CO and VOCs concentrations using a global-scale stratospheric and tropospheric

7   chemistry-climate model (MRI-CCM2; Deushi and Shibata, 2011) as the boundary conditions

8   of RAQM2.

9   Table 5 summarizes the statistical analysis for the comparison between the observation and

10   simulation of all the available data at the six EANET stations. The simulation of daily

11   maximum 8-hour mean O_3 was found to be successful, as the medians of observation and

12   simulation were close to each other and the Root Mean Square Errors (RMSEs) were much

13   lower than the medians. The correlation coefficient R is 0.47 and 96% of the data-satisfied

14   factor of 2. The R of the daily mean SO_2 and NO_x concentrations was the same as that of O_3,

15   whereas there were larger discrepancies in the medians, RMSEs, FAC2 and FAC5. Because

16   these EANET stations are located over remote ocean areas, the temporal variations of O_3

17   were always incremented by background concentrations due to the long-range transport.

18   While this smaller variation/background ratio of O_3 resulted in better scores for RMSEs,

19   FAC2 and FAC5 than SO_2 and NO_x, the same levels of R indicate that the predictability of

20   the transport patterns of the three species were similar. The simulated O_3 was not biased

21   toward the observation, but the simulated SO_2 and NO_x were biased by 30-50%.

22

23   ## 3.4   Bulk mass concentrations of aerosol chemical components

24   Fig. 3 presents a scatter diagram between the observed and modeled concentrations of

25   biweekly chemical components at the Rishiri, Oki and Hedo stations. These stations are

26   located over a wide range, from the northeast to the southwest of the Japan archipelago, so

27   different types of long-range transport patterns from the Asian continent can be evaluated. We

28   also selected these stations because the $PM_{2.5}$ mass concentrations were monitored together

29   with PM_{10} only at Rishiri and Oki and because the AMS PM_1 measurements were taken only

30   at Hedo.

The statistics of the corresponding data at all six stations are listed in Table 5. The medians of the modeled nss-SO_4^{2-} and T-NH_4^+ were approximately 30% smaller than the observed, whereas the modeled T-NO_3^- was almost double that observed. The nitric acid and ammonia are semi-volatile in atmospheric conditions and were partitioned into gas and aerosol phases. However, due to the artifact problems mentioned in Sect. 3.1, the gas-aerosol partitioning was not evaluated. The partitioning is essentially important for the transport of the species because the dry and wet deposition efficiencies of nitric acid and ammonia in gas and aerosol phases are very different (Kajino et al., 2008). The modeled gas-aerosol partitioning of the semi-volatile components should be evaluated using accurate measurements for HNO_3 and NH_3 gases in the future to identify the possible causes of the discrepancies between the model and observation. The RMSEs of nss-SO_4^{2-}, NH_4^+, and NO_3^- were comparable to the medians, and the R^2 values were always greater than 0.5.

T-Cl^- and Na^+ mainly originate from sea salt particles because the EANET stations are close to the ocean. Natural aerosols are usually difficult to simulate due to the large uncertainties in the emission flux estimations, and the Rs were lower than the other chemical components. Still, the RMSEs and modeled medians were close to the observed medians. Nss-Ca^{2+} was considered to originate from Asian dust particles, which contain calcite; these are also natural aerosols and were difficult to simulate. The modeled median was approximately double that measured. We assumed uniform compositions for dust emission from the whole model domain, which may not have been natural. Still, a large value of R was obtained for nss-Ca^{2+} because the long-range transport of Asian dust in Japan is most influential in spring, and this feature was well reproduced by RAQM2. The Rs at the western stations, where the dust transport is more frequent, were especially larger, with 0.74 and 0.76 at Hedo and Oki, respectively.

3.5 Size distributions of total aerosol mass

Fig. 4 presents the daily mean observed and modeled concentrations of PM_{10}, $PM_{2.5}$, and $PM_{2.5}/PM_{10}$ concentration ratios and modeled constituent fractions of PM_{10}, $PM_{2.5}$, and PM_1 at the Rishiri and Oki stations. $PM_{2.5}$ includes sub-micron aerosols and a portion of super-micron aerosols, such as sea salt and dust particles, so the $PM_{2.5}/PM_{10}$ ratio provided some idea of the mass size distribution of the super-micron particles or mass ratios of anthropogenic (mostly sub-micron) and natural origin aerosols (mostly super-micron) (Kajino and Kondo, 2011). Notably, the modeled $PM_{2.5}$ and PM_{10} were derived using Eq. (17) by cutting each wet

aerosol particles in a category at the exact diameter (2.5 and 10 μm, respectively), so the size classification property differed from that of the instruments, characterized by the so-called cut-off curve. As shown in Table 5, the medians of the modeled $PM_{2.5}$ and PM_{10} are 40% and 50% smaller, respectively, than the observed. The RMSEs were comparable to the median values, and approximately half of the data satisfied a factor of 2 and more than 80% satisfied a factor of 5. Notably, the statistics for PM_{10} included data from all six stations, whereas those for $PM_{2.5}$ included only those from Oki and Rishiri. The modeled and observed median of the $PM_{2.5}/PM_{10}$ ratio agreed well, as the RMSE is small and more than 80% of the data satisfied a factor of 2, except that R is almost zero. Together with the comparison shown in Figs. 4e and 4f, the daily variations of the $PM_{2.5}/PM_{10}$ ratio may have failed to be simulated, but longer-term features were well reproduced by the model. The variations of the measured ratios were not large, with the median ranging from 0.4 to 0.6. The values at Oki (0.9) in August were excluded because the measured $PM_{2.5}$ data were missing during most of the period. The modeled mean $PM_{2.5}/PM_{10}$ ratios were also within the same range of 0.4-0.6, except at Rishiri from January to March. The overestimation of the model during the period indicates that the modeled size was smaller than that observed.

The 10-d mean fractions of the PM_{10}, $PM_{2.5}$, and PM_1 constituents are also shown in Fig. 4 (g)-(l). The red, green, yellow, blue, and sky blue columns indicate the total dry mass of ATK and ACM, the total dry mass of AGR, the dust mass (DU) of COR, the sea salt mass (SS+Cl$^-$) of COR, and the other dry mass of COR, respectively. The ATK, ACM, and AGR are mainly of anthropogenic origin and are composed of submicron particles (PM_1). COR is mainly of natural origin and was partitioned into $PM_{2.5}$ and PM_{10}. The ATK, ACM, and AGR particles accounted for more than 90% of the PM_1 except in spring and autumn at Rishiri and spring at Oki. The COR particles accounted for more than 90% of the PM_{10} except in summer. The modeled fractions of ATK, ACM, and AGR in $PM_{2.5}$ and PM_{10} became larger in summer because the sea salt production and dust transport are less pronounced than those in the cold seasons. The $PM_{2.5}/PM_{10}$ ratio of the chemical components was an excellent indicator of the mixing type of the inorganic components (Kajino and Kondo, 2011), but that of the total aerosol mass was merely an indicator of the COR category sizes. The modeled fractions of the constituents of $PM_{2.5}$ and PM_{10} did not differ greatly from one another, but those of PM_1 and PM_{10} were very different. Unfortunately, we did not obtain PM_1 mass concentration data, but a comparison between the modeled and observed PM_1/PM_{10} ratio, if available, may provide additional important implications for modeling studies.

1

3.6 Size distributions and mixing types of inorganic components

3

3.6.1 Relationship between chemical size distribution and mixing types

Fig. 5 shows the observed and modeled (left) daily mean PM_1 concentrations of the nss-SO_4^{2-}, NH_4^+, NO_3^-, and Cl^- concentrations and (right) the biweekly mean bulk concentrations of nss-SO_4^{2-}, T-NH_4^+, T-NO_3^-, T-Cl^-, Na^+, and nss-Ca^{2+}. To derive the modeled PM_1 concentrations for the comparisons with the AMS data, Eq. (17) was again applied. Notably, the equation was applied for the modeled "dry" size distribution, whereas it was applied for the "wet" size distribution for the cases of $PM_{2.5}$ and PM_{10}, corresponding to the measurement techniques.

Table 6 summarizes the statistical analysis of the corresponding data shown in Fig. 5. In summer, the Pacific high is influential, carrying a clean maritime air mass to Hedo. In cold seasons, long-range transport from the Asian continent via cyclonic fronts or anticyclones propagating eastward is predominant. Therefore, the concentrations of air pollutants are low in summer and high in spring, autumn, and winter. These seasonal features and daily variations were successfully reproduced by the model. The model results of the natural aerosols, such as sea salt (Na^+) and Asian dust (Ca^{2+}), at Hedo were also successful. The transport events of the Asian dust in spring and autumn were found in both the observation and simulation.

Although the variations were well simulated, the levels were underestimated for some components, such as PM_1-nss-SO_4^{2-} and PM_1-NH_4^+. The modeled medians were approximately 30% of those observed (Table 6). The model also underestimated the bulk nss-SO_4^{2-} and T-NH_4^+, and the underestimation was consistent with that for PM_1. The underestimations of PM_1-nss-SO_4^{2-} and PM_1-NH_4^+ were most likely due to the underestimation of the bulk mass. The trends and values of PM_1-NO_3^- were well predicted by the model, whereas the T-NO_3^- was overestimated.

Fig. 6 presents the (left) biweekly mean PM_1 to the total (gas plus aerosol) concentration ratios for nss-SO_4^{2-}, T-NH_4^+, T-NO_3^-, and T-Cl^-. The observed values were depicted only when the available hourly AMS data exceeded 50% during each biweekly FP period (more than 140 hourly data out of the two weeks). The statistical values between the observed and

modeled data are listed in Table 6. Fig. 6 also presents (right) the biweekly mean fractions of gas and aerosol categories for each inorganic component. The observed median of the PM_1 to bulk $nss\text{-}SO_4^{2-}$ ratio was 0.85. The ratio exceeded 1.0 for some cases, so it may be within the uncertainties of the analysis (Fig. 6a). The modeled ratio was also large because approximately 80% of the $nss\text{-}SO_4^{2-}$ was mixed with submicron particles, such as ATK, ACM and AGR (Fig. 6b). The modeled median was 0.66, which was smaller than that observed, indicating that the modeled size distribution of $nss\text{-}SO_4^{2-}$ may have been larger than that observed or may indicate that the proportions mixed with larger COR particles might have been overestimated. The features of the NH_4^+ ratio were similar to those for $nss\text{-}SO_4^{2-}$ because $nss\text{-}SO_4^{2-}$ is a major counterpart of NH_4^+. A range of 20-60% of $T\text{-}NH_4^+$ existed in the gas phase in summer as NH_3 because the temperature was high enough for NH_4NO_3 to evaporate and/or the amount of $nss\text{-}SO_4^{2-}$ was not enough to consume NH_3 gas to fix it to the aerosol phase as ammonium sulfate. Because the modeled $nss\text{-}SO_4^{2-}$ and NH_4^+ were both underestimated, the improvement of $nss\text{-}SO_4^{2-}$ could also result in the improvement of NH_4^+.

The observed and modeled medians of the PM_1 to $T\text{-}NO_3^-$ ratios were 0.054 and 0.035, respectively, more than 1 order of magnitude smaller than those for $nss\text{-}SO_4^{2-}$ and NH_4^+ (Fig. 6e). Those are about 1 order of magnitude larger than those for the sea-salt originated components $T\text{-}Cl^-$. It indicates that some fractions of nitrate are mixed with sea-salt particles as $NaNO_3$, while the other mixed with submicron particles.as NH_4NO_3. It is discussed later more in detail in Sect. 3.6.3.

The observed and modeled medians of the PM_1 to $T\text{-}Cl^-$ ratios were one order of magnitude smaller than those for $T\text{-}NO_3^-$. Almost all (99.4% on average) of the aerosol phase Cl^- was mixed with COR particles. The modeled fractions of HCl gas showed a maximum in summer, with a value of 51%. Because anthropogenic HCl emission was not considered in the current settings of RAQM2, the modeled $T\text{-}Cl^-$ are all of sea salt origin. The temperature is high and the air is photochemically active in summer, so the HNO_3 gas concentration is also high. HNO_3 gas efficiently condensed onto sea-salt particles and expelled the Cl^- into the gas phase by the chlorine deficit reaction (Eq. 26) in summer.

3.6.2 Mixing type of sulfate

Fig. 7 illustrates spatial distribution of mean concentrations and mixing types of sulfate in lower atmosphere (<~1000m; averages in 1st to 7th vertical grids). The seasonal trends of the mixing type of nss-SO_4^{2-} were interesting (Fig.6b and Fig.7). Nss-SO_4^{2-} internally mixed with ATK + ACM was the greatest in summer (June to July; Figs.7c and 7d). Because the air is cleaner in summer, there are fewer surface areas of pre-existing aerosols for H_2SO_4 gas to condense onto, and new particle formation would occur more frequently. In contrast, in cold seasons, due to the abundance of preexisting aerosols including soot, H_2SO_4 gas was efficiently condensed onto the soot particles (AGR) (Figs.7e and 7f). However, the current analysis could not prove the plausibility of the mixing type. For this proof, the results should be evaluated in the future by comparing them with the measurements of the soot mixing state using a Volatility Tandem Differential Mobility Analyzer (VTDMA), a Single Particle Soot Photometer (SP2), or a Transmission Electron Microscope (TEM). The modeled nss-SO_4^{2-} was mixed with COR from 10-40%. The crustal components in COR, such as Na^+ in sea-salt or Ca^{2+} in Asian dust, could be counterparts of nss-SO_4^{2-}. The proportions show maxima in spring from March to May (40% in April as a maximum), which coincides with the Asian dust transport period at Hedo (Fig. 5j). In the current setting of RAQM2, unfortunately, the dust particles are categorized as COR together with sea salt particles, so we cannot evaluate nss-SO_4^{2-} mixed solely with Asian dust. Because the modeled nss-SO_4^{2-} was mixed with COR, either with sea salt or Asian dust throughout the year, the modeled PM_1 to bulk ratio was approximately 0.6. The observed ratio also sometimes dropped to the modeled levels, even less than half in May. Although certain discrepancies remained between the modeled and observed ratios, the modeled partitioning may not be so far from reality.

3.6.3 Mixing type of nitrate

Fig. 8 shows spatial distribution of mean concentrations and mixing types of nitrate in the lower atmosphere. The mixing type of NO_3^- at Hedo (Fig. 6f) was interesting when it was compared with that at Gosan, Jeju Island, Korea (shown in Fig. 1 as an arrow). The observed and modeled medians of the PM_1 to T-NO_3^- ratios were 0.054 and 0.035, respectively, more than 1 order of magnitude smaller than those for nss-SO_4^{2-} and NH_4^+ and 1 order of

1   magnitude larger than those for Cl⁻. This result means that the observed and modeled T-NO_3^-

2   partitioned into the gas phase or internally mixed with aerosols larger than PM_1 were close to

3   each other, at 94.6% and 96.5%, respectively. Kajino and Kondo (2011) made a similar

4   analysis for the case of the $PM_{2.5}/PM_{10}$ ratios of chemical components at Gosan. They

5   calculated that 53.7% of the modeled NO_3^- was internally mixed with sea salt particles on

6   average in March 2005. The value was consistent with the observation, where the mean

7   values of the modeled and observed $PM_{2.5}/PM_{10}$ ratios of NO_3^- were both 0.66. In the current

8   simulation, 98% of the NO_3^- was internally mixed with COR at the annual average at Hedo

9   (Fig. 6f). The values of Fig. 8g is larger than those of Fig. 6l of Kajino and Kondo (2011)

10   because the current figure is the average of surface to 1000 m height, while their paper

11   showed those of surface concentration, which contains more proportion of fresh sea-salt

12   particles. There are clear gradient in Fig. 8g from the upstream near the continent (~50%)

13   toward downwind over the ocean (>90%).

14   The difference of the mixing type of NO_3^- at Gosan and Hedo was explained using the

15   following equations:

16          $NH_3 \text{ (g)} + HNO_3 \text{ (g)} \leftrightarrow NH_4NO_3 \text{ (p)}$ (25)

17          $NaCl \text{ (p)} + HNO_3 \text{ (g)} \rightarrow NaNO_3 \text{ (p)} + HCl \text{ (g)}$ (26)
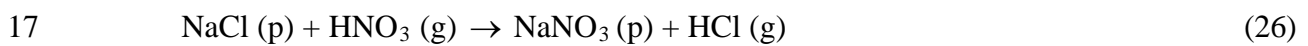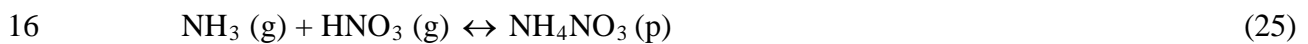
18   Gosan is located approximately 700 km upwind of Hedo, toward the Asian continent. During

19   long-range transport, HNO_3 gas is produced via the photochemical oxidation of NO_x. The

20   mass transfer coefficients for each aerosol mode of category were nearly proportional to their

21   total surface area for atmospheric aerosol size ranges (near the continuum regime). Over the

22   continent, more than 90% of the NO_3^- was mixed with submicron particles as NH_4NO_3 (Eq.

23   25; see NUC+AGR in Figs. 6j and 6k of Kajino and Kondo, 2011). We combined dust, sea-

24   salt and anthropogenic PM_{10} particles together as the COR category, there are substantial

25   proportions of nitrate mixed with COR over the continent in Fig.8g, but those are not sea-salt

26   particles. In contrast to the downwind regions of the continent over the ocean, the HNO_3 gas

27   produced during transport is more efficiently condensed to sea salt particles, as the

28   proportions of the sea salt surface area become large. The reaction of Eq. (26), occurring on/in

29   the sea salt particles, also promoted the condensation of HNO_3 onto sea salt forming $NaNO_3$.

30   Even though the HNO_3 gas production during transport is less significant, the reaction Eq.

31   (26) itself may promote the evaporation of HNO_3 gas in Eq. (25), because it is a reversible

32   reaction. In this case, the conversion of NO_3^- in submicron particles to sea salt particles might

occur. The fractions of nitrate with COR are predominant all over the ocean (>80%) in summer (Fig. 8h), as the temperature is higher and the fraction of HNO_3 gas becomes larger (Eq.25), which results in the promotion of reaction Eq.26.

~~Gosan is located approximately 700 km upwind of Hedo, toward the Asian continent. The spatial distributions of the mixing types of NO_3^- showed that more than 90% of the NO_3^- could be internally mixed with sea salt over further downwind regions such as Hedo, whereas approximately 50% is mixed with sea salt over the Yellow Sea, where Gosan is located (Fig. 6l of Kajino and Kondo, 2011).~~

The mixing type of NO_3^- may be important for the size distribution of aerosols and its light scattering property. Although the same amounts of aerosol NO_3^- existed in the air, HNO_3 condensed onto submicron particles forming NH_4NO_3, together with its water uptake, enhances the particle size efficiently and alter the light scattering property. However, HNO_3 condensed onto sea salt particles may not alter the particle size and optical property as significantly. It is because it expels HCl at the same time, the water uptake property may not change much, and the size increase ratio will be smaller than that for submicron particles as the sea salt particles are much larger.

3.6.4 Mixing type of soot aggregate and soot-coarse mode particle mixtures

Even though the simulated mixing state of soot and soot-COR mixtures were not evaluated by the measurements, we showed some examples as those are important for aerosol-radiation-cloud interaction aspects. Fig.9 illustrates mean black carbon (BC) concentration in AGR, total dry mass to BC mass ratio, and total wet mass to BC mass ratio. The SP2 measured shell/core diameter ratio in Asian continental outflow was about 1.6 (Shiraiwa et al., 2008) so the mass ratio could be around 4. Our simulated values could be significantly overestimated about 5-10 over the continent to 15-20 over the ocean (Figs 9c and 9d). The hygroscopic components mixed with AGR were simulated to uptake water about 3-4 times the original dry mass.

Fig.10 shows the mean number concentrations of soot aggregate (AGR), coarse mode particles (COR) and number of AGR collided to COR particles (M_0^{AGR} in Table 2). As discussed in Sect. 2.2.4, M_0^{AGR} does not mean the number of AGR-COR aggregate. The coalescence efficiency may not be unity and one COR particle can be attached by several AGR particles. In the simulation, M_0^{AGR} were comparable to M_0 of COR particles (~1-10

particles/cm^3), when M_0 of AGR are 2-3 orders of magnitude larger (~1000 particles/cm^3) and the BC mass concentrations are larger than 2-5 µg/m^3. When the number concentration is low in summer (Fig. 10b) due to lower emission flux and larger convection and turbulent mixing, the probability of collision between AGR and COR particles could be significantly lower (Fig. 10f).

4   Conclusions

A new aerosol chemical transport model, Regional Air Quality Model 2 (RAQM2), was developed to simulate Asian air quality. We implemented a simple version of a triple-moment modal aerosol dynamics model (MADMS; Kajino 2011) and achieved a completely dynamic (non-equilibrium) solution of a gas-to-particle mass transfer over a wide range of aerosol diameters, from 1 nm to super µm. To consider a variety of atmospheric aerosol properties, the category approach (Kajino and Kondo, 2011) is utilized. In RAQM2, aerosols are distributed into 4 categories: 1. particles in Aitken mode (ATK), 2. soot-free particles in accumulation mode (ACM), 3. soot aggregates (AGR) and 4. particles in coarse mode (COR). ~~In the current setting, aerosol size distribution in each category is characterized by a single mode. New particle formation, condensation/evaporation, and intra/inter category coagulations for each mode of categories are solved dynamically.~~ A regional-scale simulation ($\Delta x = 60$ km) was performed for the entire year of 2006 covering the northeast Asian region.

~~To evaluate the model performance on the major inorganic components in the air, we used observed hourly air concentrations of SO_2, NO_x, O_3, $PM_{2.5}$, and PM_{10}. We also used 1- or 2-weekly air concentrations of aerosol nss-SO_4^{2-}, total (gas plus aerosol) (T)-NO_3^-, T-Cl^-, T-NH_4^+, Na^+, and nss-Ca^{2+} of the Acid Deposition Monitoring Network in East Asia (EANET). Higher temporal-resolution data of aerosol components were used, and the hourly concentrations of PM_1-nss-SO_4^{2-}, PM_1-NO_3^-, PM_1-Cl^-, and PM_1-NH_4^+ were measured using a quadrupole aerosol mass spectrometer (Aerodyne Research Inc., Q-AMS) at the Cape Hedo Atmospheric and Aerosol Monitoring Station (CHAAMS). Statistical analyses showed that the model reproduced the regional-scale transport and transformation of the major inorganic anthropogenic and natural air constituents within factors of 2 to 5.~~ The modeled size distributions ($PM_{2.5}/PM_{10}$ of total weight and PM_1/bulk ratios of chemical components) agreed quantitatively with those observed at EANET and CHAAMS sites. We concluded that

our prediction of aerosol mixing types (ATK, ACM, AGR and COR) of inorganic aerosol components such as $nss\text{-}SO_4^{2-}$, NH_4^+, NO_3^-, and Cl^- were consistent with those in nature.

The modeled mixing types of the chemical components were found to be interesting. The $Nss\text{-}SO_4^{2-}$ internally mixed with ATK + ACM was greatest in summer (June to July). Because the air is cleaner in summer, there are less surface areas of preexisting aerosols for H_2SO_4 gas to condense onto; thus, new particle formation would occur more frequently. In contrast, in cold seasons, due to the abundance of pre-existing aerosols including soot, H_2SO_4 gas was efficiently condensed onto the soot particles (AGR). To evaluate the results, the modeled mixing type should be evaluated in the future by comparing it with measurements of the soot mixing state using Volatility Tandem Differential Mobility Analyzer (VTDMA), Single Particle Soot Photometer (SP2), or Transmission Electron Microscope (TEM) analysis. The simulated total dry mass to black carbon (BC) mass ratio was about 5-10 over the continent and 15-20 over the ocean, which are significantly larger than the previous measurement in Asian continental outflow (~4). Further efforts will be necessary to obtain the consistent features of Asian aerosol properties. The number of AGR collided to COR, was also simulated in this study, which could be comparable to the number concentration of COR (~1-10 particles/cm^3), when the number concentrations of AGR were 2-3 orders of magnitude larger (~1000 particles/cm^3) in cold seasons. When the concentrations of AGR were low in summer, the probability of collision between AGR and COR particles could be significantly lower.

The difference in mixing type of the NO_3^- at Hedo and Gosan was interesting. Ninety-eight percent of the modeled NO_3^- was internally mixed with COR at Hedo, whereas 53.7% of the NO_3^- was internally mixed with sea salt particles at Gosan (Kajino and Kondo, 2011). The modeled values were consistent with the observed $PM_{2.5}/PM_{10}$ ratio of the NO_3^- at Gosan and the $PM_1/T\text{-}NO_3^-$ ratio at Hedo. Gosan is located upwind of Hedo toward the Asian continent. To the downwind regions of the continent over the ocean, the HNO_3 gas produced during transport is more efficiently condensed onto sea salt particles, as the proportions of the sea salt surface area to the total aerosol surface area become large. The chlorine deficit reaction on the sea salt particles promoted the condensation of HNO_3. This reaction decreases HNO_3 gas concentration, resulting in evaporation of NH_4NO_3 from submicron particles. This conversion of nitrate in submicron particles to sea salt particles might occur during transport.

The aerosol mixing type is a key parameter for the light-scattering and absorbing properties, in addition to number, size, and chemistry. Further investigation is needed by comparing the results with aerosol optical thickness (AOT) or single scattering albedo (SSA) observations for the accurate assessment of aerosol-radiation interaction processes. It is also an essential parameter for predicting CCN and IN activities of aerosols. For the better understanding of the importance of those parameters in the whole aerosol–cloud–radiation interaction systems, online coupling of meteorology – chemistry models is indispensable in the near future.

The current model is computationally efficient in a sense that even though we consider the mixing types we need only a few numbers of transport variables as we used a modal approach, which is less accurate compared to a sectional approach. It is also efficient in aerosol process modeling because even though we used 1 s of time step to resolve the simultaneous nucleation, condensation, and coagulation processes of nano-particles, we adopted a larger time step to solve multi-component thermodynamic equilibrium state, which is computationally expensive. One box simulations with sensitivity runs (operator splitting, time splitting, number of modes or categories, or modal v.s. sectional approaches) will be useful to optimize the current method in terms of accuracy and efficiency.

References

Abdul-Razzak, H., Ghan, S. J.: A parameterization of aerosol activation. 2. Multiple aerosol typles, J. Geophys. Res., 105(D5), 6837-6844, 2000.

An, J., Ueda, H., Wang, Z., Matsuda, K., Kajino, M., Cheng, X.: Simulations of monthly mean nitrate concentrations in precipitation. Atmos. Environ., 36, 4159-4171, 2002.

An, J., Ueda, H., Matsuda, K. Hasome, H., and Iwata, M.: Simulated impacts of SO_2 emissions from the Miyake volcano on concentration and deposition of sulfur oxides in September and October of 2000. Atmos. Environ., 37, 3039-3046, 2003.

Binkowski, F. S., Shankar, U.: The regional particulate model: 1. Model description and preliminary results, J. Geophys. Res., 100, 26,191-26.209, doi:10.1029/95JD02093, 1995.

Byun, D., Schere, K. L.: Review of the governing equations, computational algorithms, and other components of the Models-3 Community Multiscale Air Quality (CMAQ) Modeling System, Applied Mechanics Reviews, 59, 51-77, 2006.

Carter, W.: Documentation of the SAPRC-99 chemical mechanism for VOC reactivity assessment. Final report to California Air Resources Board, Rep. 92-329, Univ. of Calif., Riverside, 8 May., 2000.

Carlton, A. G., Turpin, B. J., Altieri, K. E., Seitzinger, S., Reff, A., Lim, H. –J., Ervens, B.: Atmospheric oxalic acid and SOA production from glyoxal: Results of aqueous photooxidation experiment. Atmos. Environ., 41, 2007.

Carmichael, G. R., Sakurai, T., Streets, D., Hozumi, Y., Ueda, H., Park, S. U., Fung, C., Han, Z., Kajino, M., Engardt, M., Bannet, C., Hayami, H., Sartelet, K., Holloway, T., Wang, Z., Kannari, A., Fu, J., Matsuda, K., Thongboonchoo, N., Amann, M.: MICS-Asia II: the model intercomparison study for Asia phase II methodology and overview of findings, Atmos. Environ., 42, 3468-3490, 2008.

Chen, F., Dudhia, J.: Coupling an advanced land-surface/ hydrology model with the Penn State/ NCAR MM5 modeling system. Part I: Model description and implementation. Mon. Weather Rev., 129, 569-585, 2001.

Clarke, A. D., Shinozuka, Y., Kapustin, V. N., Howell, S., Huebert, B., Doherty, S., Anderson, T., Covert, D., Anderson, J., Hua, X., Moore II, K. G., McNaughton, C., Carmichael, G. R., Weber, R.: Size distributions and mixtures of dust and black carbon aerosol in Asian outflow: Physicochemistry and optical properties. J. Geophys. Res., 109, doi:10.1029/2003JD004378, 2004.

Clarke, A. D., Owens, S. R., Zhou, J.: An ultrafine sea-salt flux from breaking waves: Implications for cloud condensation nuclei in the remote marine atmosphere. J. Geophys. Res., 111, D06202, doi:10.1029/2005JD006565, 2006.

1 Deushi, M., Shibata, K.: Development of an MRI Chemistry-Climate Model ver.2 for the
2 study of tropospheric and strarospheric chemistry, Papers in Meteor. Geophys., 62, 1-46, 2011.

3 DOE, 1994: Handbook of methods for the analysis of the various parameters of the carbon
4 dioxide system in sea water. Version 2, A. G. Dickson and C. Goyet, eds., ORNL/CDIAC-74,
5 1994.

6 Dudhia, J.: Numerical study of convection observed during the winter monsoon experiment
7 using a mesoscale two-dimensional model. J. Atmos. Sci., 46, 3077-3107, 1989.

8 Edney, E. O., Kleindienst, T. E., Lewandowski, M., Offenberg, J. H.: Updated SOA chemical
9 mechanism for the Community Multiscale Air Quality model. EPA 600/X-07/025, U. S.
10 Environ. Prot. Agency, Durham, N. C., 2007.

11 Foley, K. M., Roselle, S. J., Appel, K. W., Bhave, P. V., Pleim, J. E., Otte, T. L., Mathur, R.,
12 Sarwar, G., Young, J. O., Gilliam, R. C., Nolte, C. G., Kelly, J. T., Gilliland, A. B., Bash, J.
13 O.: Incremental testing of the Community Multiscale Air Quality (CMAQ) modeling system
14 version 4.7, Geosci. Model Dev., 3, 205-226, 2010.

15 Fountoukis, C., Nenes, A.: ISORROPIA II: a computationally efficient thermodynamic
16 equilibrium model for K^+-Ca^{2+}-Mg^{2+}-NH_4^+-Na^+-SO_4^{2-}-NO_3^--Cl^--H_2O aerosols, Atmos. Chem.
17 Phys., 7, 4639-4659, 2007.

18 Fuchs, N.A.: The Mechanics of Aerosols, Pergamon Press, Oxford, 1964.

19 Giglio, L., Randerson, J. T., van der Werf, G. R., Kasibhatla, P. S., Collatz, G. J., Morton, D.
20 C., Defries, R. S.: Assessing variability and long-term trends in burned area by merging
21 multiple satellite fire products. Biogeosciences, 7, 1171-1186, 2010.

22 Grell, G. A., Devenyi, D.: A generalized approach to parameterizing convection combining
23 ensemble and data assimilation techniques. Geophys. Res. Lett. 20(14), 1693,
24 doi:10.1029/2002GL015311, 2002.

25 Guazzotti, S. A., Coffee, K. R., Prather, K. A.: Continuous measurements of size-resolved
26 particle chemistry during INDOEX-Intensive Field Phase 99. J. Geophys. Res., 106, 28,607-
27 28,628, 2001.

28 Guenther, A., Karl, T., Harley, P., Wiedinmyer, C., Palmer, P. I., Geron, C.: Estimates of
29 global terrestrial isoprene emissions using MEGAN (Model of Emissions of Gases and
30 Aerosols from Nature). Atmos. Chem. Phys., 6, 3181-3210, 2006.

Han, Z., Ueda, H., Matsuda, K., Zhang, R., Arao, K., Kanai, Y., Hasome, H.: Model study on particle size segregation and deposition during Asian dust events in March 2002. Journal of Geophysical Research 109, D19205, doi:10.1029/2004JD004920, 2004.

Han, Z., Ueda, H., Matsuda, K.: Model study of the impact of biogenic emission on regional ozone and effectiveness of emission reduction scenarios over eastern China, Tellus B, 53, 171-191, 2005.

Han, Z., Ueda, H., Sakurai, T.: Model study on acidifying wet deposition in East Aisa during wintertime, Atmos. Environ., 40, 2360-2373, 2006.

Han, Z.: A regional air quality model: evaluation and simulation of O_3 and relevant gaseous species in East Asia during spring 2001, Environ., Modell., Softw., 22, 1328-1336, 2007.

Hirsikko, A., Nieminen, T., Gagne, S., Lehtipalo, K., Manninen, H. E., Ehn, M., Hõrrak, U., Kerminen, V.-M., Laakso, L., McMurry, P. H., Mirme, A., Mirme, S., Petäjä, T., Tammet, H., Vakkari, V., Vana, M., Kulamala, M.: Atmospheric ions and nucleation: a review of observations. Atmos. Chem. Phys., 11, 767-798, 2011.

Hong, S. –Y., Lin, J. –O. J.: The WRF single-moment 6-class microphysics scheme (WSM6), J. Korean Meteor. Soc. 42, 129-151, 2006.

Ishikawa, H.: Mass-consistent wind model as a meteorological preprocessor for tracer transport models, J. Appl. Meteorol., 33, 733-743, 1994.

Jacobson, M. Z., Ginnebaugh, D. L.: Global-through-urban nested three-dimensional simulation of air pollution with a 13,600-reaction photochemical mechanism. J. Geophys. Res., 115, D14304, doi:10.1029/2009JD013289, 2010.

Janjic, Z. I.: Nonsingular implementation of the Mellor-Yamada level 2.5 scheme in the NCEP Medo model, Off. Note, 437, 61 pp., Natl. Cent. for Environ. Predict., Camp Springs, Md.

Kajino, M., Ueda, H., Satsumabayashi, H., An, J.: Impacts of the eruption of Miyakejima Volcano on air quality over far east Asia, J. Geophys. Res., 109, D21204, doi:10.1029/2004JD004762, 2004.

Kajino, M., Ueda, H., Satsumabayashi, H., Han, Z.: Increase in nitrate and chloride deposition in east Asia due to increased sulfate associated with the eruption of Miyakejima Volcano, J. Geophys. Res., 110, D18203, doi:10.1029/2005JD005879, 2005.

Kajino, M., Ueda, H., Nakayama, S.: Secondary acidification: Changes in gas-aerosol partitioning of semivolatile nitric acid and enhancement of its deposition due to increased emission and concentration of SO_x. J. Geophys. Res., 113, D03302, doi:10.1029/2007JD008635, 2008.

Kajino, M.: MADMS: Modal Aerosol Dynamics model for multiple Modes and fractal Shapes in the free-molecular and near-continuum regimes. J. Aerosol Sci., 42, 224-248, 2011.

Kajino, M., Kondo, Y.: EMTACS: Development and regional-scale simulation of a size, chemical, mixing type, and soot shape resolved atmospheric particle model. J. Geophys. Res., 116, D02303, doi:10.1029/2010JD015030, 2011.

Kang, J.-Y., Yoon, S.-C., Shao, Y., Kim, S.-W.: Comparison of vertical dust flux by implementing three dust emission schemes in WRF/Chem., J. Geophys. Res., 116, D09202, doi:10.1029/2010JD014649, 2011.

Katata, G., Nagai, H., Wrzesinsky, T., Klemm, O., Eugster, W., Burkard, R.: Development of a land surface model including cloud water deposition on vegetation, J. Appl. Meteor. Climatol., 47, 2129-2146, 2008.

Katata, G., Nagai, H., Zhang, L., Held, A., Serça, D., Klemm, O.: Development of an atmosphere-soil-vegetation model for investigation of radioactive materials transport in the terrestrial biosphere, Prog. Nucl. Sci. Technol., 2, 530-537, 2011 (online available: http://www.aesj.or.jp/publication/pnst002/data/530-537.pdf).

Kirsch, A.A., Fuchs, N.A.: Studies on fibrous aerosol filters. III . Diffusional deposition of aerosols in fibrous filters, Ann. Occup. Hyg., 11, 299-304, 1968.

Kuang, C., McMurry, P. H., McCormick, A. V., Eisele, F. L.: Dependence of nucleation rates on sulfuric acid vapor concentration in diverse atmospheric locations. J. Geophys. Res. 113, D10209, doi:10.1029/2007JD009253, 2008.

Kulmala, M., Kerminen, V.-M.: On the formation and growth of atmospheric nanoparticles. Atmos. Res., 90, 132-150, 2008.

Kurokawa, J., Ohara, T., Uno, I., Hayasaka, M., Tanimoto, H.: Influence of meteorological variability on interannual variations of springtime boundary layer ozone over Japan during 1981-2005. Atmos. Chem. Phys., 9, 6287-6304, 2009.

1 Lin, Y. –L., Farley, R. D., Orville, H. D.: Bulk parameterization of the snow field in a cloud
2 model. J. Clim. Appl. Meteorol., 22, 1065-1092, 1983.

3 Lohmann, U., Diehl, K.: Sensitivity studies of the importance of dust ice nuclei for the
4 indirect aerosol effect on stratiform mixed-phase clouds. J. Atmos. Sci., 63, 968-982, 2010.

5 Madronich, S.: Photodissociation in the atmosphere: 1. Actinic flux and the effects of ground
6 reflections and clouds. J. Geophys. Res., 92, 9740-9752, doi:10.1029/JD092iD08p09740,
7 1987.

8 Mlawer, E. J., Taubman, S. J., Brown, P. D., Iacono, M. J., Clough, S. A.: Radiative transfer
9 for inhomogeneous atmosphere, RRTM, a validated correlated-k model for the long wave, J.
10 Geophys. Res., 102, 16,663-16,682, doi:10.1029/97JD00237, 1997.

11 Myneni, R. B., Hoffman, S., Knyazikhin, Y., Privette, J. L., Glassy, J., Tian, Y., Wang, Y.,
12 Song, X., Zhang, Y., Smith, G. R., Lotsch, A., Friedl, M., Morisette, J. T., Votava, P., Nemani,
13 R. R., Running S. W.: Global products of vegetation leaf area and fraction absorbed PAR
14 from year one of MODIS data. Remote Sensing of Environment, 83, 214-231, 2002.

15 Nagashima, T., Ohara, T., Sudo, K., Akimoto, H.: The relative importance of various source
16 regions on East Asian surface ozone. Atmos. Chem. Phys., 10, 11,305-11,322, 2010.

17 Ohara, T., Akimoto, H., Kurokawa, J., Horii, N., Yamaji, K., Yan, X., Hayasaka, T.: An
18 Asian emission inventory of anthropogenic emission sources for the period 1980-2020. Atmos.
19 Chem. Phys., 7, 4419-4444, 2007.

20 Peters, K., Eiden, R.: Modelling the dry deposition velocity of aerosol particles to a spruce
21 forest, Atmos. Environ., 26A, 2555-2564, 1992.

22 Petroff, A., Zhang, L.: Development and validation of a size-resolved particle dry deposition
23 scheme for application in aerosol transport models, Geosci. Model Dev., 3, 753-769, 2010.

24 Pleim, J. E., Chang, J. S.: A non-local closure model for vertical mixing in the convective
25 boundary layer. Atmos. Environ., 26A, 965-981, 1992.

26 Pruppacher, H. R., Klett, J. D.: Microphysics of Clouds and Precipitation, Kluwer Acad.,
27 Norwell, Mass., 1997.

28 Sekiyama, T. T., Tanaka, T. Y., Shimizu, A., Miyoshi, T.: Data assimilation of CALIPSO
29 aerosol observations., Atmos. Chem. Phys. 10, 39-49, 2010.

Shiraiwa, M., Kondo, Y., Moteki, N., Takegawa, N., Sahu, L. K., Takami, A., Hatakeyama, S., Yonemura, S., Blake, D. R.: Radiative impact of mixing state of black carbon aerosol in Asian outflow, J. Geophys. Res., 11, D24210, doi:10.1029/2008JD010546, 2008.

Skamarock, W. C., Klemp, J. B., Dudhia, J., Gill, D. O., Barker, D. M., Duda, M. G., Huang, X. Y., Wang, W., Powers, J. G.: A description of the advanced research WRF version 3, Tech. Note, NCAR/TN~475+STR, 125 pp., Natl. Cent. for Atmos. Res., Boulder, Colo., 2008.

Song C. H., Carmichael, G. R.: A 3D modeling investigation of the evolution processes of dust and sea-salt particles in east Asia. J. Geophys. Res., 106(D16) 18,131 – 18,154, 2001.

Sudo, K., Akimoto, H.: Global source attribution of tropospheric ozone: Long-range transport from various source regions. J. Geophys. Res., 112, D12302, doi:10.1029/2006JD007992, 2007.

Takami, A., Miyoshi, T., Shimono, A., Kaneyasu, N., Kato, S., Kajii, Y., and Hatakeyama, S.: Transport of anthropogenic aerosols from Asia and subsequent chemical transformation. J. Geophys. Res., 112, D22S31, doi:10.1029/2006JD008120, 2007.

Takiguchi, Y., Takami, A., Sadanaga, Y., Lun, X., Shimizu, A., Matsui, I., Sugimoto, N., Wang, W., Bandow, H., and Hatakeyama, S.: Transport and transformation of total reactive nitrogen over the East China Sea. J. Geophys. Res., 113, D10306, doi:10.1029/2007JD009462, 2008.

Walcek, C. J., Aleksic, N. M.: A simple but accuate mass conservative peak-preserving, mixing ratio bounded advection algorithm with fortran code. Atmos. Environ., 32, 3863-3880, 1998.

Walcek, C. J., Teylor, G. R.: A theoretical method for computing vertical distributions of acidity and sulfate production within cumulus clouds. J. Atmos. Sci., 43, 339-355, 1986.

Wang, Z., Akimoto, H., Uno, I.: Neutralization of soil aerosol and its impact on the distribution of acid rain over east Asia: Observations and model results, J. Geophys. Res., 107, D19, 4389, doi:10.1029/2001JD001040, 2002.

Whitby, E. R., McMurry, P. H.: Modal aerosol dynamics modeling, *Aerosol Sci. Technol*, 27, 673-688, 1997.

Yang, W., Shabanov, N. V., Huang, D., Wang, W., Dickinson, R. E., Nemani, R.R., Knyazikhin, Y., Myneni, R. B.: Analysis of leaf area index products from combination of MODIS Terra and Aqua data, Remote Sensing of Environment, 104, 297-312, 2006.

Yumimoto, K., Uno, I., Sugimoto, N., Shimizu, A., Liu, Z., Winker, D.M.: Adjoint inversion modeling of Asian dust emission using lidar observations, Atmos. Chem. Phys. 8, 2869-2884, 2008.

Zhang, L., Gong, S., Padro, J., Barrie, L.: A size-segregated particle dry deposition scheme for an atmospheric aerosol module. Atmos. Environ., 35, 549-560, 2001.

Zhang, L., Brook, J. R., Vet, R.: A revised parameterization for gaseous dry deposition in air-quality models. Atmos. Chem. Phys., 3, 2067-2082, 2003.

Zhang, Q., Streets., D. G., Carmichael, G. R., He, K. B., Huo, H., Kannari, A., Klimont, Z., Park, L. S., Reddy S., Fu, J. S., Chen, D., Duan, L., Lei, Y., Wang, L. T., Yao, Z. L.: Asian emission in 2006 for the NASA INTEX-B mission. Atmos. Chem. Phys., 9, 5131-5133, 2009.

Zhang, Y., McMurry, P. H., Yu, F., Jacobson, M. Z.: A comparative study of nucleation parameterizations: 1. Examination and evaluation of the formulations. J. Geophys. Res., 115, D20212, doi:10.1029/2010JD014150, 2010.

Zhu, A., Ramanathan, V., Li, F., Kim, D.: Dust plumes over the Pacific, Indian and Atlantic Oceans: Climatology and radiative impact. J. Geophys. Res., 112, doi:10.1029/2007JD008427, 2007.

1 **Table 1.** List of data and schemes used in the WRF and RAQM2 models

Scheme	Name / reference
WRF	
Initial and boundary conditions, analysis nudging	National Center for Environmental Prediction (NCEP) final operational global analysis data (available from http://dss.ucar.edu/datasets/ds083.2)
Planetary boundary layer	Mellor-Yamada-Janjic (MYJ) model (Janjic, 2002)
Grid-scale cloud microphysics parameterization	The six-class scheme WSM6 (Lin et al, 1983)
Subgrid-scale cumulus parameterization	Grell and Devenyi (2002)
Land surface model	Noah LSM (Chen and Dudhia, 2001)
Long-wave radiation	RRTM (Mlawer et al., 1997)
Short-wave radiation	Dudhia (1989)
RAQM2	
Boundary condition of O_3 and its precursors	MRI-CCM2 (Deushi and Shibata, 2011) climatological value
Emission (anthropogenic, biogenic, open biomass burning, mineral dust, sea-salt)	REAS (Ohara et al., 2007; Kurokawa et al., 2009), GFED3(Giglio et al., 2010), MEGAN2 (Guenther et al., 2006), Asian dust (Han et al., 2004), Sea-salt (Clarke et al., 2006)
Advection	MPMAA (Walcek and Aleksic, 1998)
J-value	Madronich (1987) with TOMS O3 column data (available from ftp://toms.gsfc.nasa.gov)
Gas chemistry	72 species and 214 reactions (SAPRC99; Carter, 2000)
SOA chemistry	Edney et al. (2007)
Liquid chemistry	Walcek and Taylor (1986); Carlton et al. (2007)
New particle formation	Kuang et al. (2008)
Aerosol dynamics (condensation, evaporation, coagulation)	This study and MADMS (Kajino, 2011)
Surface gas-aerosol equilibrium of inorganic and organic compounds	ISORROPIA2 (Fountoukis and Nenes, 2007), Edney et al. (2007)
Dry deposition	This study and Zhang et al. (2001), (2003), Katata et al. (2008), (2011)
CCN activation	Abdul-Razzak and Ghan (2000)
IN activation	Lohmann and Diehl (2010)
Grid-scale cloud microphysics	Lin et al. (1983)
Collision of aerosol to grid-scale rain, snow and graupel droplets	This study
Sub-grid-scale convection and wet deposition	ACM (Pleim and Chang, 1992)

Table 2. Aerosol categories and transported variables in the RAQM2 model

Category number	Category name	Physical components		Chemical compositions									
1	ATK	M_0	M_2	-	-	-	-	-	SO_4^{2-}	NH_4^+	NO_3^-	Cl^-	H_2O
2	ACM	M_0	M_2	UID	-	OA	-	-	SO_4^{2-}	NH_4^+	NO_3^-	Cl^-	H_2O
3	AGR	M_0	M_2	UID	BC	OA	-	-	SO_4^{2-}	NH_4^+	NO_3^-	Cl^-	H_2O
4	COR	M_0	M_2	UID	BC	OA	DU	SS	SO_4^{2-}	NH_4^+	NO_3^-	Cl^-	H_2O
		M_0^{AGR}											

Table 3. Rules for transfer of the three moments and chemical mass concentrations from one

category to another due to inter-category coagulation and mode merging

Rule Number	Rule
	Inter-category Coagulation
1	1.ATK + 2.ACM → 2.ACM
2	1.ATK + 3.AGR → 3.AGR
3	1.ATK + 4.COR → 4.COR
4	2.ACM + 3.AGR → 3.AGR
5	2.ACM + 4.COR → 4.COR
6	3.AGR + 4.COR → 4.COR
	Mode Merging
7	(swelling) 1.ATK → 2.ACM
8	(shrinking) 2.ACM → 1.ATK

1 **Table 4.** Description of the EANET remote sites and the CHAAMS site used in this study.

2 Each station is depicted in Figure 1.

	Longitude (E)	Latitude (N)	Altitude (m a.s.l.)	Character-istics	X	Y	MT	AT	AT-PM$_{2.5}$	FP	AMS
1. Rishiri	141º12'	45º07'	40	Remote	68	48	1h	1h	1h	2w	N.A.
2. Tappi	140º21'	41º15'	105	Remote	69	41	1h	1h	N.A.	2w	N.A.
3. Ogasawara	142º13'	27º05'	230	Remote	77	16	1h	1h	N.A.	1w	N.A.
4. Sado	138º24'	38º14'	136	Remote	67	35	1h	1h	N.A.	2w	N.A.
5. Oki	133º11'	36º17'	90	Remote	60	30	1h	1h	1h	2w	N.A.
6. Hedo & CHAAMS	128º15'	26º52'	60	Remote	54	12	1h	1h	N.A.	2w	1h

3 X,Y: Model grid number; MT: meteorological parameters, AT: automatically monitored

4 (NO$_x$, O$_3$, SO$_2$, PM$_{10}$; PM$_{2.5}$ is only available at Rishiri and Oki), FP: filter pack method

5 (Aerosol inorganic components), AMS: aerosol mass spectrometer, only available at

6 CHAAMS. CHAAMS is located within the same premises as the EANET Hedo station. 1h:

7 hourly, 1w: weekly, 2w: 2 weekly.

8

9

10

11

12

13

14

15

16

17

18

19

20

1 **Table 5.** Statistical analysis for comparison between all EANET data of observation and
2 simulation for 2006.

	Unit	Number of data	Median (Obs.)	Median (Sim.)	RMSE	R	FAC2[a]	FAC5[b]
Daily mean bulk gas concentrations (AT[d])								
O_3[c]	ppbv	2093	50.3	51.2	16.9	0.47	0.96	1.00
SO_2	ppbv	2052	0.17	0.25	0.70	0.52	0.36	0.64
NO_x	ppbv	1819	0.80	0.58	1.1	0.49	0.52	0.86
1- or 2-weekly bulk concentrations of chemical compounds (FP[e])								
$Nss\text{-}SO_4^{2-}$	$\mu g\ m^{-3}$	152	1.9	1.3	1.9	0.70	0.46	0.80
$T\text{-}NH_4^+$	$\mu g\ m^{-3}$	138	0.71	0.45	0.69	0.52	0.50	0.81
$T\text{-}NO_3^-$	$\mu g\ m^{-3}$	144	0.92	1.8	2.2	0.59	0.47	0.87
$T\text{-}Cl^-$	$\mu g\ m^{-3}$	144	3.7	2.8	4.2	0.13	0.42	0.89
Na^+	$\mu g\ m^{-3}$	144	2.3	1.4	2.5	0.13	0.38	0.85
$Nss\text{-}Ca^{2+}$	$\mu g\ m^{-3}$	152	0.056	0.11	0.24	0.55	0.38	0.67
Daily mean $PM_{2.5}$ and PM_{10} concentration and their ratios (AT)								
$PM_{2.5}$	$\mu g\ m^{-3}$	696	8.8	5.2	10.8	0.45	0.52	0.87
PM_{10}	$\mu g\ m^{-3}$	2141	17.7	8.3	19.1	0.65	0.45	0.81
$PM_{2.5}/PM_{10}$	-	674	0.57	0.49	0.26	0.018	0.83	1.00

3   a.   Fraction of data that satisfy a factor of 2.

4   b.   Fraction of data that satisfy a factor of 5.

5   c.   Daily maximum 8 hour mean.

6   d.   Measured by automatic instruments.

7   e.   Measured by the filter pack method.

8

9

10

11

12

1 **Table 6.** Statistical analysis for comparison between observation and simulation at the Hedo

2 EANET and CHAAMS stations.

	unit	Number of data	Median (Obs.)	Median (Sim.)	RMSE	R	FAC2	FAC5
Daily PM$_1$ concentrations (AMS[a])								
PM$_1$-nss-SO$_4^{2-}$	µg m^{-3}	199	4.2	1.3	4.4	0.57	0.28	0.72
PM$_1$-NH$_4^+$	µg m^{-3}	199	1.0	0.34	1.0	0.56	0.28	0.70
PM$_1$-NO$_3^-$	µg m^{-3}	199	0.088	0.080	0.15	0.30	0.53	0.90
PM$_1$-Cl$^-$	µg m^{-3}	197	0.027	0.016	0.088	0.097	0.26	0.58
2-weekly bulk concentrations of chemical compounds (FP[b])								
Nss-SO$_4^{2-}$	µg m^{-3}	22	5.9	2.0	3.0	0.83	0.32	0.86
T-NH$_4^+$	µg m^{-3}	20	1.4	0.47	0.91	0.56	0.20	0.80
T-NO$_3^-$	µg m^{-3}	22	1.7	2.6	1.7	0.49	0.72	1
T-Cl$^-$	µg m^{-3}	22	8.2	2.8	5.6	0.35	0.22	0.86
Na$^+$	µg m^{-3}	22	5.1	1.6	3.6	0.30	0.22	0.86
Nss-Ca^{2+}	µg m^{-3}	22	0.14	0.11	0.19	0.74	0.55	0.81
2-weekly PM$_1$ to total concentration ratios (AMS/FP)								
Nss-SO$_4^{2-}$	-	12	0.85	0.66	0.32	-	0.92	1
T-NH$_4^+$	-	12	0.81	0.71	0.26	-	0.92	1
T-NO$_3^-$	-	12	0.054	0.035	0.027	-	0.75	1
T-Cl$^-$	-	12	0.0038	0.0080	0.0082	-	0.33	0.67

3 a. Measured by quadrupole aerosol mass spectrometer (Aerodyne Research Inc., Q-AMS)

4 b. Measured by the filter pack method.

5

6

7

8

9

10

1   **Figure 1.** Model domain showing terrestrial elevation (m) and the six Japanese EANET sites
2   (1. Rishiri, 2. Tappi, 3. Ogasawara, 4. Sado, 5. Oki, 6. Hedo) and the CHAAMS sites (located
3   in the same premises as the EANET Hedo stations). The descriptions of the locations are
4   given in Table 4. An arrow indicates the Gosan site on Jeju Island, Korea.

5

6   **Figure 2.** Schematic illustration of (a) operator splitting and time splitting for the RAQM2
7   aerosol dynamics module and (b) changes in moments and LNSD parameters when passing
8   each process operator.

9

10 **Figure 3.** Scatter diagram between observed and modeled concentrations of biweekly (a)-(c)
11 nss-SO_4^{2-}, (d)-(f) T-NH_4^+, (g)-(i) T-NO_3^-, (j)-(l) Na^+, and (m)-(o) nss-Ca^{2+} at (left) Rishiri,
12 (center) Oki and (right) Hedo. Solid lines denote the 1:1 line, and dashed lines denote the
13 factor of 2 envelope.

14

15 **Figure 4.** Daily mean observed (blue) and modeled (red) concentrations of (a)-(b) PM_{10}, (c)-
16 (d) $PM_{2.5}$, (e)-(f) $PM_{2.5}/PM_{10}$ concentration ratios (the median with 75 and 25 percentile
17 values) and modeled constituent fractions of (g)-(h) PM_{10}, (i)-(j) $PM_{2.5}$, and (k)-(l) PM_1
18 concentrations at (left) Rishiri and (right) Oki. Among the constituents, ATK+ACM (red) is
19 the total dry mass (SO_4^{2-}, NH_4^+, NO_3^-, Cl^-, UID and OA) of the ATK and ACM categories,
20 AGR (green) is the total dry mass (UID, BC, OA, SO_4^{2-}, NH_4^+, NO_3^-, and Cl^-) of the AGR
21 category, COR-DU (yellow) is the dust mass (DU) of the COR category, COR-SS (blue) is
22 the sea-salt mass (SS+Cl^-) in the COR category and COR-Other (sky blue) is the other
23 components (UID, BC, OA, SO_4^{2-}, NH_4^+, and NO_3^-) in the COR category.

24

25 **Figure 5.** (Left) daily mean AMS measured (blue, left axis) and modeled (red, right axis)
26 PM_1 (a) nss-SO_4^{2-}, (c) NH_4^+, (e) NO_3^-, and (g) Cl^- concentrations at Hedo (CHAAMS).
27 (Right) biweekly FP measured and modeled (b) nss-SO_4^{2-}, (d) T-NH_4^+, (f) T-NO_3^-, (h) T-Cl^-,
28 (i) Na^+, and (j) nss-Ca^{2+} concentrations at Hedo (EANET).

29

Figure 6. (Left) biweekly mean PM_1 to total (gas plus aerosol) concentration ratios and (Right) the modeled fractions of gas phase (grey), ATK+ACM category (red), AGR category (green), and COR category (blue) aerosols of (a)-(b) nss-SO_4^{2-}, (c)-(d) T-NH_4^+, (e)-(f) T-NO_3^-, and (g)-(h) T-Cl^- at Hedo.

Figure 7. Spatial distributions of mean concentrations and mixing types of sulfate in lower atmosphere (<~1000m) in (left) March and (right) July. (a)-(b) sulfate concentration ($\mu m/m^3$), (c)-(d) fraction of sulfate mixed with non-light-absorbing particles (ATK + ACM) (%), (e-f) fraction of sulfate mixed with light-absorbing particles (AGR) (%).

Figure 8. Spatial distributions of mean concentrations and mixing types of nitrate in lower atmosphere (<~1000m) in (left) March and (right) July. (a)-(b) total-nitrate (gas plus aerosol) concentration ($\mu m/m^3$), (c)-(d) nitric acid gas concentration ($\mu m/m^3$), (e)-(f) fraction of nitrate mixed with submicron particles (ATK + ACM + AGR) (%), (g)-(h) fraction of nitrate mixed with coarse mode particles (COR) (%).

Figure 9. Spatial distributions of mean concentrations and mixing types of black carbon in lower atmosphere (<~1000m) in (left) March and (right) July. (a)-(b) black carbon concentration ($\mu m/m^3$), (c)-(d) dry mass to black carbon mass ratio (-), (e)-(f) wet mass to black carbon mass ratio (-).

Figure 10. Spatial distributions of mean number concentrations in (left) March and (right) July of (a)-(b) soot (particles/cm^3), (c)-(d) coarse mode particles (dust, sea-salt, and anthropogenic PM_{10}) (particles/cm^3) and (e)-(f) number of soot aggregate collided with coarse mode particles (particles/cm^3).